

1 Simulating the unsteady stable boundary layer with a 2 stochastic stability equation

3 Vyacheslav Boyko¹ and Nikki Vercauteren^{2,3}

4 ¹Department of Mathematics and Computer Sciences, Freie Universität Berlin, Berlin, Germany

5 ²Department of Geosciences, University of Oslo, Oslo, Norway

6 ³Institute for Geophysics and Meteorology, University of Cologne, Cologne, Germany

7 **Key Points:**

- 8 • A stochastic parameterization of turbulence is implemented in a Reynolds aver-
- 9 age Navier-Stokes (RANS) model to represent unsteady mixing.
- 10 • The introduced stochastic perturbations of the mixing length enable the simula-
- 11 tion of intermittent turbulence in the stable boundary layer.
- 12 • The stochastic unsteady RANS model does not alter the simulation of neutral con-
- 13 ditions.

14 **Abstract**

15 Turbulence in stable boundary layers is typically unsteady and intermittent. The study
 16 implements a stochastic modelling approach to represent unsteady mixing possibly as-
 17 sociated with intermittency of turbulence and with unresolved fluid motions such as dirty
 18 waves or drainage flows. The stochastic parameterization is introduced by randomizing
 19 the mixing lengthscale used in a Reynolds average Navier-Stokes (RANS) model with
 20 turbulent kinetic energy closure, resulting in a stochastic unsteady RANS model. The
 21 randomization alters the turbulent momentum diffusion and accounts for sporadic events
 22 of possibly unknown origin that cause unsteady mixing. The paper shows how the pro-
 23 posed stochastic parameterization can be integrated into a RANS model used in weather-
 24 forecasting and its impact is analyzed using neutrally and stably stratified idealized nu-
 25 matical case studies. The simulations show that the framework can successfully model
 26 intermittent mixing in stably stratified conditions, and does not alter the representation
 27 of neutrally stratified conditions. It could thus present a way forward for dealing with
 28 the complexities of unsteady flows in numerical weather prediction or climate models.

29 **Plain Language Summary**

30 Limited computer resources lead to a simplified representation of unresolved small-
 31 scale processes in weather forecasting and climate models, through parameterization schemes.
 32 Among the parameterised processes, turbulent fluxes exert a critical impact on the ex-
 33 change of heat, water and carbon between the land and the atmosphere. Turbulence the-
 34 ory was, however, developed for homogeneous and flat terrain, with stationary conditions.
 35 At nighttime or in cold environment, turbulence is typically non-stationary, weak and
 36 intermittent and the classical theory fails. Part of the intermittent mixing is due to tur-
 37 bulence enhancement by small-scale wind variability. In the following, a random mod-
 38 ellng approach is used to enhance turbulent mixing due to small-scale wind variability
 39 and intermittency of mixing. The proposed approach is shown to be a viable approach
 40 to represent the effect of small-scale variability of mixing for different atmospheric flow
 41 conditions.

42 **1 Introduction**

43 The representation of the atmospheric boundary layer in stably stratified condi-
 44 tions is an intricate problem for numerical weather prediction (NWP) and climate mod-
 45 els (Holtslag et al., 2013; Sandu et al., 2013). Stably stratified conditions can occur at
 46 nighttime when radiative cooling of the surface is predominant, or when warm air is ad-
 47 vected over a cold surface, for example over snow or ice. Such conditions favour model
 48 biases, a prominent example being systematic errors in the near-surface temperature (Davy
 49 & Esau, 2014; Esau et al., 2018; Køltzow et al., 2019). The different processes occurring
 50 at the interface between the surface and the lower atmosphere interact in complex ways,
 51 making the identification of the main source of error challenging. Model errors have been
 52 related to shortcomings in the calculation of turbulent fluxes, radiative fluxes or ground
 53 heat fluxes, as well as to an overestimated heat capacity of a too deep boundary layer,
 54 preventing a sufficiently fast reaction of the near-surface temperature (Tjernström et al.,
 55 2005; Sandu et al., 2013; Esau et al., 2018).

56 Turbulence in the stable boundary layer (SBL) is generated by shear production,
 57 while its development is inhibited by buoyant forces. Due to this interplay, flow regimes
 58 with different physical and dynamical characteristics exist (van de Wiel & Moene, 2003;
 59 Mahrt, 2014). Fully turbulent SBL, also coined as weakly stable boundary layers, are
 60 rather well described by similarity theory, but the very stable boundary layer with in-
 61 termittent turbulence is less well understood (Grachev et al., 2005; Mahrt, 2014; LeMone
 62 et al., 2018). At high stability, non-turbulent processes become more important, and the
 63 flow is characterised by strong non-stationarity (Mahrt & Bou-Zeid, 2020). For exam-

ple, larger scale wave-like motions can interact in complex ways and contribute to intermittent turbulence (Cava et al., 2019). Non-turbulent flow features smaller than those traditionally classified as mesoscales, denoted as submesoscale motions, exist under all atmospheric stratifications for weak winds (Anfossi et al., 2005), but exert a critical influence under strong stratification. In these conditions characterised by a large Richardson number, turbulence production is closely related to local short-term accelerations associated with submeso motions (Mahrt, 2011; Boyko & Vercauteren, 2020; Lan et al., 2022). Approaches to parameterise non-turbulent motions are being developed, including the quasi-normal scale elimination (QNSE, Sukoriansky et al. (2005)) that includes breaking gravity waves, or a quantification of wave drag due to small scale orography (Steeneveld et al., 2009). Another closure approach is based on the total turbulent energy that considers the potential energy due to density fluctuations of the fluid in addition to the traditional consideration of turbulent kinetic energy (Zilitinkevich et al., 2007; Mauritsen et al., 2007). A unified treatment of non-stationary turbulence in very stable conditions is however lacking (LeMone et al., 2018; Edwards et al., 2020).

With weak winds and clear-sky conditions, associated with strong stability, the atmosphere may become decoupled from the surface (Acevedo et al., 2016). This occurs when a layer near the surface becomes driven by radiation and soil thermal transport, while the surface turbulent heat flux is too weak to sustain the energy demand of the surface (Van de Wiel et al., 2012). In NWP, the decoupling can occur in very localised regions with a high spatial variability, and the positive feedback between weakening turbulence and radiative cooling can lead to further rapid cooling in decoupled regions (Kähnert et al., 2022). To avoid such decoupling and so-called runaway cooling to become unphysically important in models, operational parameterisation schemes have implemented rather high levels of turbulent mixing (Louis, 1979; Derbyshire, 1999; Cuxart et al., 2006). This practice is often justified by the need to account for the numerous processes impacting mixing that are not resolved in NWP and climate models, such as unresolved surface heterogeneity or topography, and internal gravity waves. This enhancement of turbulent mixing is typically calibrated to reduce the activity of synoptic systems and improve model scores, with the negative consequence that NWP and climate models simulate too deep boundary layers, too weak low-level jets or wind veering with height (Sandu et al., 2013).

In an effort to model the variability of mixing related to intermittency of turbulence, internal or related to submeso motions, Boyko and Vercauteren (n.d.) devised a stochastic extension to MONIN–OBUKHOV Similarity Theory (MOST) that is able to model intermittent turbulent bursts. The proposed approach keeps the physical basis of MOST untouched, assuming a gradient-diffusion model in which the diffusivity scales with an appropriate lengthscale incorporating the influence of dimensionless stability. It extends MOST by treating the stability correction and thus the mixing lengthscale as a time-continuous stochastic variable, thereby enabling the representation of unsteady mixing. There may be intrinsic limits in such a gradient-diffusion model structure, even when the diffusion coefficient is stochastic, however turbulence parameterisation schemes used in operational NWP models were shown to reasonably capture the physics of the SBLs for a variety of forcing provided they do not apply excessive vertical mixing (Cuxart et al., 2006; Baas et al., 2018, 2019). Using tools from uncertainty quantification, Audouin et al. (2021) concluded that model deficiencies reflect a poor parameterization calibration rather than intrinsic limits of the parameterization formulation. These authors further suggested a framework combining single-column models and large eddy simulations to improve the calibration of SBL model parameters. In the observational study presented in Boyko and Vercauteren (n.d.), the calibration of a proposed time continuous stochastic stability equation is analysed statistically using field observations and inverse modelling methods. The results highlight scaling of the stochastic model parameters with dimensionless atmospheric stability, providing a closed-form parametrisation of turbulence that enables explicit treatment of the uncertainty of the fluxes to be modelled. Due to the time-continuous model structure, the proposed stochastic extension of MOST en-

ables the representation of localised bursts of turbulence through a stochastic model. Such a stochastic parameterisation of turbulence can provide much needed uncertainty estimations, and may also be needed to better represent the mean state and SBL regime transitions that can occur via inherent nonlinear processes (Berner et al., 2017; Van de Wiel et al., 2017).

In this study, the stochastic representation of the mixing length is implemented into a REYNOLDS-averaged NAVIER–STOKES (RANS) model. The momentum and heat diffusivity, as well as all the state variables are predicted from a stochastic mixing length according to the stochastic stability equation introduced by Boyko and Vercauteren (n.d.). The fact that stochastic perturbations are introduced enables intermittency to be modeled. The study investigates the impact of the suggested stochastic scheme on a range of numerical case studies to evaluate the robustness of the proposed framework. The stochastic model, coined as Stochastically Unsteady REYNOLDS-averaged NAVIER–STOKES Equations (SURANS), is presented in section 2 and its numerical implementation in introduced in section 3. Section 4 presents the results of numerical case studies, which include a neutrally stratified boundary layer, a stably stratified boundary layer, followed by a case with variable geostrophic wind and radiative forcing. A summary and conclusions are given in section 5.

2 A Stochastic Model of the Unsteady Stable Boundary Layer

2.1 Deterministic model

For a flat surface in a dry atmosphere, assuming horizontal homogeneity, neglecting radiative flux divergence, applying the BOUSSINESQ approximation, and using a turbulence closure model based on eddy diffusivities (where $\overline{w'w'} = -K_m \frac{\partial u}{\partial z}$, $\overline{w'v'} = -K_m \frac{\partial v}{\partial z}$, and $\overline{w'\theta'} = -K_h \frac{\partial \theta}{\partial z}$), the idealised Stable Boundary Layer (SBL) can be represented by the following RANS model (Stull, 1988):

$$\frac{\partial u}{\partial t} = (v - v_g)f_c + \frac{\partial}{\partial z} \left(K_m \frac{\partial u}{\partial z} \right) \quad (1)$$

$$\frac{\partial v}{\partial t} = -(u - u_g)f_c + \frac{\partial}{\partial z} \left(K_m \frac{\partial v}{\partial z} \right) \quad (2)$$

$$\frac{\partial \theta}{\partial t} = \frac{\partial}{\partial z} \left(K_h \frac{\partial \theta}{\partial z} \right) \quad (3)$$

$$\frac{d\theta_g}{dt} = \frac{1}{C_g} (R_n - H_0) - \kappa_m (\theta_g - \theta_s) \quad (4)$$

where u, v are the mean (Reynolds averaged) horizontal wind components and θ is the mean potential temperature. The horizontal pressure gradient is prescribed through the geostrophic velocity above the SBL, whose wind components are (u_g, v_g) , and f_c is the CORIOLIS parameter. The ground surface temperature θ_g is the bottom boundary condition of Eq. (3) and its evolution is modeled using a force-restore method (Stull, 1988; Garratt, 1994; Acevedo et al., 2021). The thermal capacity of the soil per unit area is denoted with C_g . The soil heat transfer coefficient $\kappa_m = 1.18\omega$ is related to the Earth's angular frequency ω . $H_0 = \rho c_p \overline{w'\theta'_0}$ is the surface sensible heat flux, where ρ is the air density and c_p is the specific heat of air at constant pressure, and R_n is the net radiation. The temperature below the surface θ_s at some finite depth is nearly constant and fluctuates on a seasonal scale. It is, therefore, deemed fixed for the simulation of individual nights.

Closing the model requires further specification of the eddy diffusivities K_m and K_h . Many operational NWP schemes use first-order schemes, in which the eddy diffusivity depends on the wind speed, a specified mixing lengthscale and a stability function (Cuxart et al., 2006). Higher-order schemes add more prognostic equations to the model

to compute turbulent quantities. A common choice is that of a 1.5 order closure, in which a prognostic equation is used only for the evolution of the Turbulence Kinetic Energy (TKE), e . In this case, which will be further developed in the following model extension, the eddy diffusivity for momentum is expressed as follow:

$$K_m = \alpha l_m \sqrt{e} \quad (5)$$

$$\frac{\partial e}{\partial t} = P_e + \frac{\partial}{\partial z} \left(K_m \frac{\partial e}{\partial z} \right) - \epsilon, \quad (6)$$

(7)

where l_m stands for the momentum mixing length and α is a modelling constant (Cuxart et al., 2006; Rodrigo & Anderson, 2013). In the evolution equation for e , Eq. (6), P_E represents the production of TKE and ϵ its dissipation rate. Turbulent kinetic energy is produced through wind shear and buoyancy, hence

$$P_e = -\overline{u'w'} \frac{\partial u}{\partial z} - \overline{v'w'} \frac{\partial v}{\partial z} + \frac{g}{\Theta_0} \overline{w'\theta'} = K_m \left[\left(\frac{\partial u}{\partial z} \right)^2 + \left(\frac{\partial v}{\partial z} \right)^2 \right] - \frac{g}{\Theta_0} K_h \frac{\partial \theta}{\partial z}. \quad (8)$$

where $g = 9.81 \text{ m s}^{-2}$ is the gravitational acceleration, $\Theta_0 = 300 \text{ K}$ is a reference potential temperature. The dissipation rate ϵ is modelled using a dissipation length l_ϵ , which is assumed equal to the mixing length in our study, i.e. $l_\epsilon = l_m$, leading to

$$\epsilon = \frac{(\alpha_\epsilon e)^{3/2}}{l_m} \quad (9)$$

where α_ϵ is a modelling constant set to $\alpha_\epsilon = 0.1$ in this study (Cuxart et al., 2006; Rodrigo & Anderson, 2013). The turbulent PRANDTL number $Pr_t = \frac{K_m}{K_h}$ can be used to obtain K_h from K_m and in the following, it is set to one for simplicity. A detailed presentation of several operational 1.5 order schemes can be found in Cuxart et al. (2006), where it can be seen that schemes differ in the values selected for the constants, in the parameterisation used for the mixing lengths and in the stability functions used to scale the eddy diffusivities according to the static stability.

2.2 Stochastic Extension

The model extension implemented in this work, denoted as SURANS model, is developed as a set of prognostic equations for simulating unsteady intermittent turbulent mixing in the SBL. The main difference to the RANS model is a stochastic extension of MOST in the form of a Stochastic Stability Equation (SSE) representing the evolution of a stability correction variable. The SSE derives from a data-driven modelling approach introduced by Boyko and Vercauteren (n.d.) with the goal of modelling the variability of turbulent fluxes due to the influence of unresolved submesoscale motions and more generally to turbulence intermittency. The SSE is limited at this stage of research to the near-surface boundary layer where field observations were analysed, and hence the following numerical implementation is meant to serve as a proof-of-concept where the effect of intermittent mixing is modeled to a certain maximum height above the surface. The impact of such a modelling strategy is analysed based on selected numerical case studies. The height-limited implementation is chosen because the SSE was calibrated based on measurements up to 30 m at one field site (Boyko & Vercauteren, n.d.). The set of equations forming the SURANS model complements the model (1)–(6) as follows:

$$\frac{\partial u}{\partial t} = (v - v_g) f_c + \frac{\partial}{\partial z} \left(K_m(\phi) \frac{\partial u}{\partial z} \right) - N_u \quad (10)$$

$$\frac{\partial v}{\partial t} = -(u - u_g) f_c + \frac{\partial}{\partial z} \left(K_m(\phi) \frac{\partial v}{\partial z} \right) - N_v \quad (11)$$

$$\frac{\partial \theta}{\partial t} = \frac{\partial}{\partial z} \left(K_h(\phi) \frac{\partial \theta}{\partial z} \right) \quad (12)$$

$$\frac{\partial e}{\partial t} = \frac{\partial}{\partial z} \left(K_m(\phi) \frac{\partial e}{\partial z} \right) + K_m(\phi) \left[\left(\frac{\partial u}{\partial z} \right)^2 + \left(\frac{\partial v}{\partial z} \right)^2 \right] - \frac{g}{\Theta_0} K_h(\phi) \frac{\partial \theta}{\partial z} - \frac{(\alpha_\varepsilon e)^{3/2}}{l_m(\phi)} \quad (13)$$

$$\frac{d\theta_g}{dt} = \frac{1}{C_g} (R_n - H_0) - \kappa_m (\theta_g - \theta_s) \quad (14)$$

$$d\phi = \tau_h^{-1} (1 + \Lambda(Ri)\phi - \mathcal{V}(Ri)\phi^2) dt + \tau_h^{-1/2} \Sigma(Ri)\phi dW_t \quad (15)$$

The SSE as equation (15) is the novel contribution to the classical RANS model and implements a time varying stochastic stability correction variable ϕ introduced in Boyko and Vercauteren (n.d.) and which will be discussed further below. Relaxation terms $N_u = (u - u_g)/\tau_r$ and $N_v = (v - v_g)/\tau_r$ are added to the momentum equations in (10) and (11), where τ_r is the relaxation time. Those nudge the solution towards the geostrophic wind and are used to damp inertial oscillations that become too important when turbulent mixing is weak, which is likely unphysical. The value of τ_r is set in a range of 3–6 hours, such that the solution is largely controlled by (10)–(15) and only mildly nudged towards the geostrophic forcing (u_g, v_g) . The prognostic Eq. (13) describes the evolution of the TKE according to the model introduced in section 2.1. Next, the gradient Ri number is used:

$$Ri = \frac{\frac{g}{\Theta_0} \frac{\partial \theta}{\partial z}}{\left(\frac{\partial u}{\partial z} \right)^2 + \left(\frac{\partial v}{\partial z} \right)^2}, \quad (16)$$

The eddy diffusivities $K_m = K_h$ are modelled according to Eq. (5) with a parameterised turbulent mixing length. The chosen parameterisation is similar to the analytical expression suggested by Blackadar (1962) for neutral ABLs, and extended by Delage (1974) to account for stability:

$$l_m = \frac{\kappa z}{\varphi(t, Ri) + \frac{\kappa z}{\lambda_b}}, \quad (17)$$

where κ is the von Kármán constant and with the difference that $\varphi(t, Ri)$, which will be properly defined in equation (21), follows from the SSE and thus is a nondimensional stochastic process that replaces the use of the dimensionless shear in the original formulation (see eg. Rodrigo and Anderson (2013), Eq.18). Following Rodrigo and Anderson (2013), the value λ_b , which restrains the size of the largest turbulent eddies in neutral stratification is parametrized as:

$$\lambda_b = 2.7 \times 10^{-4} \frac{u_g}{|f_c|}, \quad (18)$$

where $f_c = 2\omega \sin(\varphi)$, with $\varphi = 40^\circ\text{N}$ and $\omega = 7.27 \times 10^{-5} \text{s}^{-1}$. The stochastic variable $\varphi(t, Ri)$ is constructed using a mixture of deterministic and stochastic formalism. Equation (15) determines the stability correction value ϕ from the surface up to some chosen height z_s (set as $z_s = 50 \text{ m}$), above which a traditional scaling function $\phi_f(Ri)$ is in operation, here taken as (Cuxart et al., 2006):

$$\phi_f(Ri) = 1 + 12Ri \quad \text{for } z > z_s. \quad (19)$$

Finally, the descriptions above and below z_s are joined through the logistic sigmoid function:

$$\text{sig}(z) = \frac{1}{1 + \exp(-k_s(z - z_s))}, \quad (20)$$

where z_s is the sigmoid's midpoint, and $k_s = 0.1$ is the steepness of the curve, which regulates the sharpness of transition from ϕ to ϕ_f at the height z_s . Then the linear-convex composite is defined:

$$\varphi(t, Ri) = \phi_f(Ri)\text{sig}(z) + \phi(t, Ri)(1 - \text{sig}(z)), \quad (21)$$

and is inserted into (17). Due to the stochasticity of φ , the mixing length l_m and hence the entire turbulence closure become stochastic. The stochastic process accounts for the variation of the mixing length hypothesised to be related to intermittency of turbulence and to submesoscale mixing events (Boyko & Vercauteren, n.d.).

The stochastic process ϕ is expressed by the prognostic Eq. (15) with the data-driven scaling functions obtained in Boyko and Vercauteren (n.d.) that scale the model coefficients with the Ri number:

$$\Lambda(Ri) = 9.3 \tanh[0.9 \log_{10}(Ri) - 0.1] + 8.3, \quad (22)$$

$$\mathcal{V}(Ri) = 10^{(0.4 \log_{10}(Ri) + 0.2)}, \quad (23)$$

$$\Sigma(Ri) = 10^{(0.8 \tanh[0.6 \log_{10}(Ri) - 0.8] + \sigma_s)}, \quad (24)$$

where σ_s (see Eq. (24)) regulates the intensity of the stochastic component of Eq. (15). The parameter σ_s can be adjusted in the range $[-1, 0]$. The value $\sigma_s = -1$ equals to the considerably low intensity of the noise, such that the solution of Eq. (15) becomes nearly deterministic. The value $\sigma_s = 0$ corresponds to the level of the Fluxes Over Snow Surfaces Phase II (FLOSS2) dataset and models relatively intense perturbations. All details related to the data-driven identification of the scaling function are given in Boyko and Vercauteren (n.d.) and are not repeated here. An example realisation of the stochastic stability equation for different levels of σ_s can be visualised in that paper, Figure 6. Finally, the data-driven identification of the parameters was done based on hourly time units. The constant $\tau_h = 3600$ in Eq. (15) transforms the units of the equation into seconds for the numerical implementation. Consider that due to $\mathbb{E}(dW_t)^2 = dt$, the process dW_t has the units of $\sqrt{\text{time}}$ (Horsthemke, 1984), and hence the transformation of units for the noise (stochastic) term is different than in the drift (deterministic) term.

3 Numerical Implementation

3.1 Discretisation

Equations (10) – (15) are discretized and solved using the Finite Element Method (FEM) library FEniCS (Alnæs et al., 2015; Logg et al., 2012), which performs the discretization of the nonlinear system using the FEM. Dunbar et al. (2008) also applied the FEM to simulate the SBL and showed that an adaptive grid refinement approach significantly increases the accuracy of the solution. Nevertheless, the adaptive grid technique is not used here. Instead, a fine grid resolution is set and found to be affordable for the single-column proof-of-concept study done here. Equation (14) is discretized with the explicit EULER method in time. The stochastic Eq. (15) is discretized with the MILSTEIN method in time (Lord et al., 2014).

Two different numerical grids are used in the discretization. For the variables u, v, θ , and e , a power-three transform on the z -axis is imposed to improve the resolution of the gradients in the vicinity of the surface. Such a non-equidistant grid cannot be used to solve the stochastic Eq. (15) due to the sampling algorithm, which utilizes a FOURIER transform. The FOURIER transform is used because the sampling procedure of the noise process uses a correlation lengthscale, such that the random perturbations are correlated in space. The interested reader is referred to Boyko (2022) for full details on this implementation and on the definition of the correlation lengthscale. Furthermore, since the stochastic perturbations are included in the lower portion of the boundary layer ($z < 50$ m) the stochastic grid is confined to the lower portion of the computational domain.

This saves computational resources and improves the vertical resolution of the stochastic perturbations. Figure 1 shows the description of the numerical grids along with the computation steps to obtain the hybrid stochastic mixing length correction φ defined by (21).

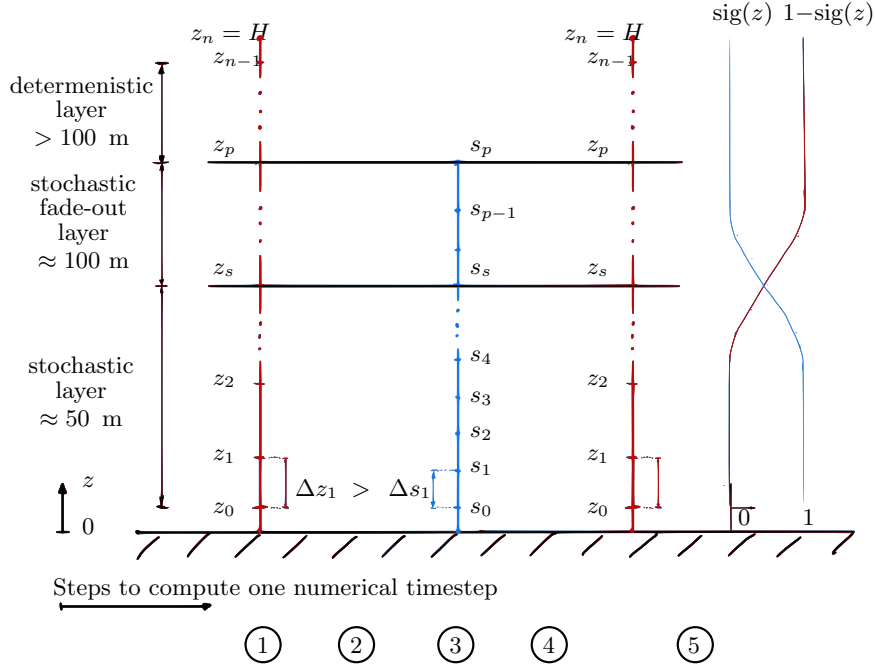


Figure 1. The computation of the hybrid stochastic mixed length correction φ using two different grids. The z -grid in red is non-equidistant and is used to solve the variables u, v, θ, e . The s -grid in blue is equidistant and is used to solve the stochastic variables ϕ . The circled numbers below mark the five steps to calculate the value of φ . 1) Calculate the Ri number on the grid z . 2) Interpolate the Ri number on the equidistant s -grid. 3) Evolve the stochastic variable ϕ to the next time step by solving the SSE. 4) Interpolate ϕ to the non-equidistant grid within the height z_p . 5) Compute the liner-convex combination between the deterministic ϕ_f and stochastic ϕ variables on the z grid using the sigmoid function $\text{sig}(z)$ (see Eq. (20)).

214

The total domain is organized into three sub-layers, as indicated on the left in Fig. 1. The stochastic layer reaches up to the height $z_s = 50$ m. In this sub-domain, the dynamic of the stability correction variable is entirely determined by the Stochastic Differential Equation (SDE) (15). From the height of z_s up to the height $1.2z_s < z_p < 2.0z_s$, the stochastic fade-out layer is defined. The layer is responsible for the smooth transition from the stochastic to the deterministic value. The transition layer is also responsible for providing sufficient buffer length needed by the sampling algorithm to obtain random structures which do not re-enter the domain at the surface s_0 . Indeed, without a buffer layer, the stochastic structures would re-enter at the surface due to periodicity assumptions of the Fourier transform used to sample to stochastic process. A linear-convex combination is performed between the stochastic ϕ and the deterministic ϕ_f variables (see Eq. (21); also marked in Fig. 1 with the step 5). The height $z_s = 50$ m characterizes the smooth blending between stochastic ϕ and the deterministic ϕ_f variables. Its value is set slightly larger than the measurement tower that was used to calibrate the stochastic part of the model. Hence, only the lowest 50 m of the simulations have a randomized stability correction in the application of MOST.

231 **3.2 Initial and boundary conditions**

Initial conditions are set following logarithmic profiles in neutral conditions, with:

$$u(z, t = 0) = \frac{u_{*,\text{init}}}{\kappa} \ln(z/z_0), \quad (25)$$

$$v(z, t = 0) = 0, \quad (26)$$

where $u_{*,\text{init}} = (0.5 C_f u_g^2)^{1/2}$. Here $C_f \approx 4 \times 10^{-4}$ is a tuning parameter and is adjusted such that u_g is obtained at the model top. The initial profile for e is estimated following Parente et al. (2011):

$$e(z, t = 0) = a_1 \ln(z) + a_2 \quad (27)$$

The coefficients a_1 and a_2 are estimated using the following boundary values:

$$e(z = z_0, t = 0) = u_{*,\text{init}}^2 (0.087)^{-1/2}, \quad (28)$$

$$e(z = H, t = 0) = 0, \quad (29)$$

where H is the domain height. The initial profile of the potential temperature is constant $\Theta_0 = 300\text{ K}$ up to a certain height $H_c = 200\text{ m}$ and then increases according to the dry adiabatic lapse rate $\Gamma = 0.01\text{ K m}^{-1}$ as used by Sorbjan (2012):

$$\theta(z, t = 0) = \begin{cases} \Theta_0, & \text{for } z \leq H_c, \\ \Theta_0 + \Gamma z, & \text{for } z \geq H_c. \end{cases} \quad (30)$$

Regarding the boundary conditions, for the wind components no-slip conditions (DIRICHLET condition) are set at the surface, while at the top boundary, the vertical gradients are set to zero (NEUMANN condition). A lapse rate is imposed as upper boundary condition for the potential temperature. The values of parameters of the SURANS model used in the numerical case studies are summarized in Tab. 1.

232 **4 Numerical Case Studies**

233 Idealised numerical case studies are used to test the SURANS model, validate the
 234 numerical stability of the proposed stochastic turbulence closure scheme and study the
 235 resulting differences to the classical RANS model with a 1.5 order closure. The impact
 236 of the stochastic perturbations that induce intermittency and unsteady mixing is anal-
 237 ysed by comparison to the unperturbed model in three numerical experiments differing
 238 in stability conditions. The neutral stratification is studied first. This study is a valida-
 239 tion case where no stability correction is needed for the mixing length, hence the ensem-
 240 ble mean of the SURANS model should match the RANS model. Next, the strongly SBL
 241 with intermittent mixing is analyzed. The SURANS model reproduces an intermittent
 242 TKE state. When analyzing this intermittent state, the ensemble mean is not a repre-
 243 sentative measure due to non-Gaussian statistics. A more appropriate measure is the cen-
 244 tral tendency (the most probable value), and its evolution is used to evaluate the per-
 245 formance of the models. Those two studies are performed for a quasi-stationary case, where
 246 the geostrophic forcing and the soil properties are constant in time. The stochastic per-
 247 turbations may also alter the solution under conditions with variable forcing, and this
 248 aspect is analyzed in a third numerical study.

249 **4.1 Neutral Boundary Layer**

250 As a first numerical experiment, a neutral boundary layer is simulated with the SURANS
 251 model. This experiment validates that the central tendency of the SURANS model, i.e.
 252 the most probable value of an ensemble of realisations, is equivalent to the RANS so-
 253 lution. The initial conditions are set as neutral profiles as described in Sec. 3 and the

Table 1. Summary of the parameter values of the SURANS solver. The parameters marked with ‘–’ are given individually in the following case studies.

Description	Symbol	Value	Source
Total simulation time [h]	T_end_h	–	set
Timestep [s]	dt	–	tuned
Grid resolution (z grid)	Nz	100	set
Roughness length [m]	z_0	0.044	(Acevedo et al., 2021)
Roughness length for heat [m]	z_{0h}	$z_0 \times 0.1$	(Sanz Rodrigo et al., 2017)
Domain height [m]	H	300	set
Restoring temperature [K]	θ_g	290	set
Reference potential Temperature [K]	Θ_0	300	set
Air density [kg/m^3]	ρ	1.225	set
Air specific heat capacity [$\text{J}/\text{kg}/\text{K}$]	c_p	1005	set
Soil heat capacity [$\text{J}/\text{m}^2/\text{K}$]	C_g	1.79e5	(Acevedo et al., 2021)
Net radiation	R_n	–	(Acevedo et al., 2021)
Geostrophic wind [m/s]	u_g	–	set
Geostrophic wind [m/s]	v_g	0	set
Latitude [$^\circ\text{N}$]	φ	40	FLOSS2 dataset
CORIOLIS parameter [rads/s]	f_c	9.34e-05	FLOSS2 dataset
Atmospheric lapse rate [K/m]	Γ	0.01	(Rodrigo & Anderson, 2013)
Relaxation time scale [s]	τ_r	3600 \times 5	tuned
Minimum TKE level [m^2/s^2]	min_tke	10^{-4}	tuned
Turbulent PRANDTL number for BC	Pr_t	0.85	(Želi et al., 2019)
Eddy viscosity constant [–]	α	0.46	(Rodrigo & Anderson, 2013)
Dissipation constant [–]	α_ε	0.1	tuned
Sub-mesoscale intensity [–]	σ_s	-0.07	FLOSS2 dataset
Stochastic model height [m]	z_s	50	FLOSS2 dataset
Covariance length [m]	l_z	20	FLOSS2 dataset
Von Kármán’s constant [–]	κ	0.41	(Rodrigo & Anderson, 2013)

Table 2. Relevant solver settings for the numerical study of the neutral layer.

Description	Symbol	Value
Total simulation time [h]	T_end_h	15
Time step [s]	dt	10
Grid resolution (z grid)	Nz	100
Domain height [m]	H	300
Restoring temperature [K]	θ_s	300
Reference potential Temperature [K]	Θ_0	300
Net radiation [W m^{-2}]	R_n	0
Geostrophic wind [m/s]	u_g	5

simulation period is set to 15 hours. The solver specific settings for this experiment are given in Tab. 2 and the rest in Tab. 1. The forcing parameters are set to be constant. The stratification is controlled with two parameters of the surface energy balance implemented in Eq. (14), namely the net radiation R_n , and the restoring temperature θ_s , which together control the degree of surface cooling. To simulate neutral conditions the net radiation is set to 0, hence forbidding radiative cooling. The restoring temperature θ_s is set equal to the initial air temperature, ensuring strictly neutral stratification.

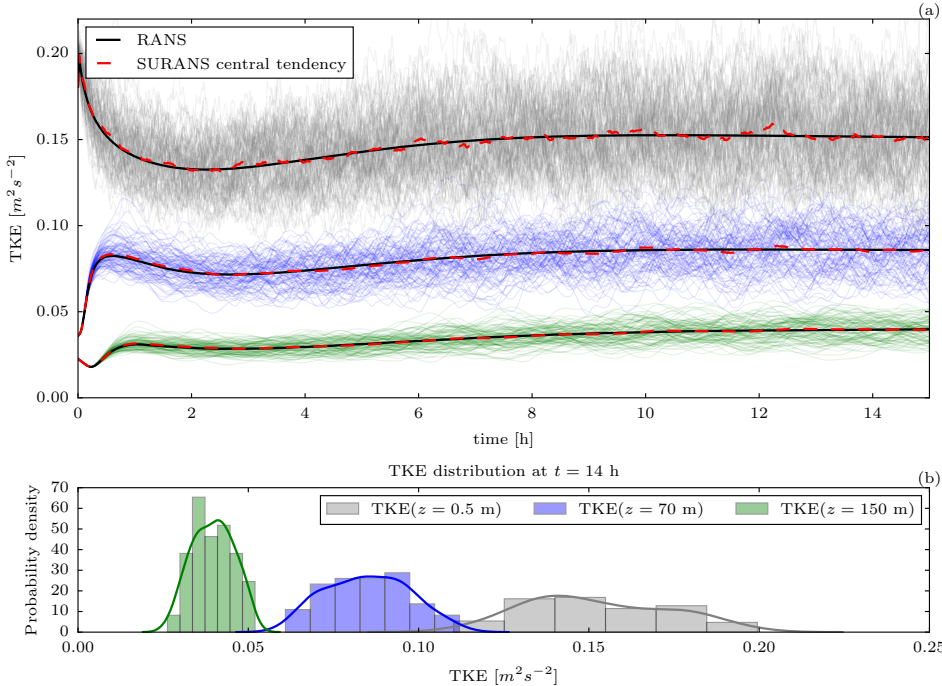


Figure 2. Comparison of the predicted TKE by the SURANS and RANS models in the condition of neutral stratification ($Ri = 0$) for three heights ($z = 0.5, 70, 150\text{ m}$). The evolution of TKE is shown in (a) and the corresponding color legend is given in (b). Panel (a) shows the RANS solution with a solid black line. The many lines in different colors indicate the 100 realizations of the SURANS model for their heights. The central tendency of the SURANS model is indicated by a dashed red line. The respective probability distribution of the TKE ensemble at $t = 14\text{ h}$ is given in panel (b).

Figure 2 shows the comparison of the TKE at three different heights ($z = 0.5, 70, 150\text{ m}$) for simulations with and without the stochastic mixing induced by the stochastic stability equation. A quasi steady-state solution is reached approximately after six hours with the RANS model. The central tendency of the SURANS model, which is estimated from averaging over 100 realizations, is nearly identical to the solution of the RANS model. The regularity of the sample paths (indicated with the thin colored lines) varies across the height. More rapid fluctuations are found closer to the surface (sample paths in gray), and smooth oscillations with smaller variances occur at $z = 150\text{ m}$ (sample paths in green). The stochastic mixing length equation is only active up to the height $z = 100\text{ m}$. As indicated by the sample paths in green ($z = 150\text{ m}$), the variability induced at the surface is propagating into the upper levels of the boundary layer. Hence the stochastic MOST impacts the upper boundary layer.

The distributions of the TKE from the 100 SURANS simulations are close to being Gaussian, but more importantly, those are symmetrical. This symmetry indicates that the modeled type of turbulence is such that the perturbed solutions maintain their path around the central tendency, which itself is very close to the deterministic RANS solution. Hence in this neutral case, the stochastically added effect of unresolved random mixing events is small enough that the TKE remains in statistical equilibrium in the perturbed model. As shown in the next stably stratified experiments, the equilib-

285 rium becomes weaker and more sensitive to the perturbations at a larger Ri number, leading
286 to turbulence intermittency.

287 4.2 Stably Stratified Boundary Layer

288 The next experiment considers a stably stratified boundary layer in the presence
289 of random mixing events. Similar to the neutral case, the initial conditions are given in
290 Sec. 3, and the simulation period is set to 15 hours. The solver-specific settings for this
291 experiment are given in Tab. 3 and the rest in Tab. 1. The forcing parameters are set
to be constant. The stratification is imposed with two mechanisms, the first being the

Table 3. Relevant solver settings for the numerical study of the stably stratified boundary layer.

Description	Symbol	Value
Total simulation time [h]	T_end_h	15
Time step [s]	dt	5
Grid resolution (z grid)	Nz	100
Domain height [m]	H	300
Restoring temperature [K]	θ_s	290
Reference potential Temperature [K]	Θ_0	300
Net radiation [W m^{-2}]	R_n	-30
Geostrophic wind [m/s]	u_g	5

292 difference between the restoring (soil) temperature of 290 K and the potential temper-
293 ature of the air 300 K, and the second being a radiative cooling enhancing the stratifi-
294 cation. The net radiation of -30 W m^{-2} is selected following Acevedo et al. (2021) and
295 considered as the FLOSS2 dataset average value. This setup may describe a typical cloud-
296 free night in springtime.

297 Figure 3 illustrates the solution of the SURANS model. The TKE at the height
298 $z = 20 \text{ m}$ is compared against the solution of the RANS model using several statisti-
299 cal metrics. In Fig. 3a, a characteristic signature of intermittent TKE simulated with
300 the SURANS model is highlighted in blue. Thin gray lines display other realizations of
301 the stochastic model. Note the two different types of spikes found at $t = 6 \text{ h}$ and $t =$
302 10 h . Their magnitude is significantly larger than the ensemble mean (solid yellow) and
303 the central tendency (solid red). The duration of these events is approximately one hour
304 and falls within the characteristic range of sub-mesoscale motions (Mahrt, 2014; Vercauteren
305 et al., 2016).

307 The ensemble mean TKE of the simulations, shown in Fig. 3, is slightly above the
308 RANS prediction. However, the central tendency is significantly smaller and indicates
309 that it is likely to observe an absence of turbulent mixing. The heavy tail in the ensem-
310 ble distributions is significant and related to sporadic rare events. Some realizations of
311 the model (not shown) predict a low TKE level throughout the entire simulation period.
312 The wide variety of TKE signatures highlights the representative capabilities of the stochas-
313 tic model. The central tendency is estimated based on the TKE distribution obtained
314 through 100 model runs at $t = 14 \text{ h}$ and shown in Fig. 3b. The solid black line repre-
315 sents the prediction of the RANS model for comparison. The solid yellow line is the en-
316 semble mean of the SURANS model, and the solid red line is the central tendency. The
317 central tendency is estimated from the Probability Density Function (PDF), which is fit-
318 ted to the histogram by applying the KDE method (Scott, 2015). The estimation is poor
319 and violates the boundary condition on the left side. Nevertheless, the KDE is a time-
320 efficient method to approximate the most probable value. The histogram indicates a smaller

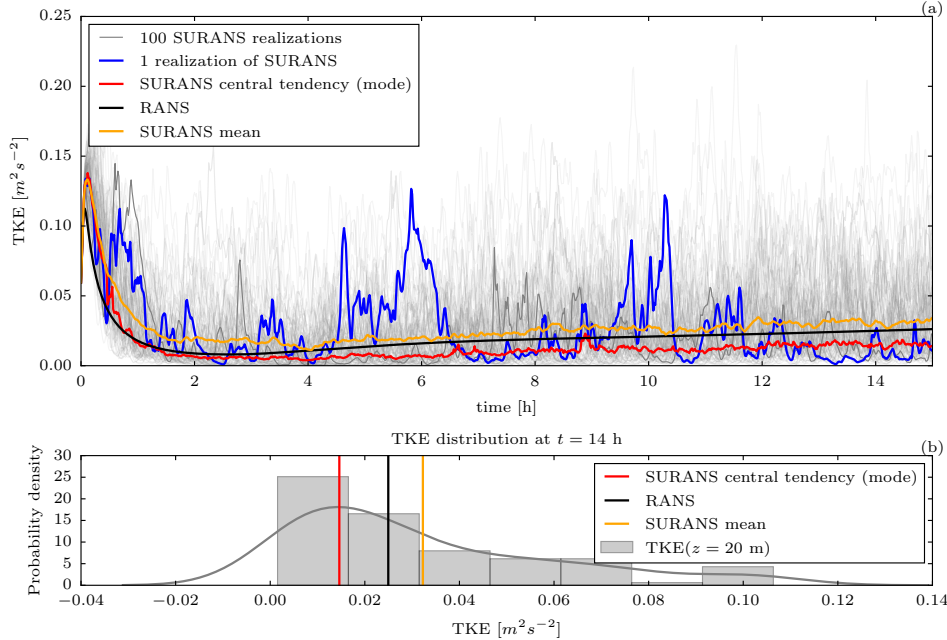


Figure 3. Comparison of SURANS and RANS models predicted TKE under the condition of strongly stable stratification (mass $Ri \approx 0.6$) for height $z = 20 \text{ m}$. For the visualization of the Ri number profiles, see Fig. 7. The evolution of the TKE is shown in (a). The ensemble distribution of 100 sample paths of the SURANS model at $t = 14 \text{ h}$ is shown in panel (b) along with the fitted probability density function (solid gray line) using a KDE method. The thin gray lines show the 100 realizations of the SURANS model.

value of the central tendency than the estimated one. A better estimation can be achieved if a specific distribution type is assumed. However, one should keep in mind that the distribution type is influenced by the stratification. This dependence makes the fitting task less trivial and we refrain from using more complex estimation approaches for studying the distributions of the TKE.

Figure 4 shows a selected realisation of the ensemble of simulations including clearly intermittent features. The largest intensity of each burst of TKE is found at the surface. The stochastic correction of the turbulent diffusion can in principle lead to intermittent patches detached from the ground (see Fig. 6 in Boyko and Vercauteren (n.d.) for such an example), as is found to occur in observations (see eg. Sun et al. (2002)). Still, in the simulation we cannot find any turbulent patches that are clearly detached from the surface. The bursts are absent aloft because the turbulent diffusion is multiplied with the gradient of the mean wind, and hence the spatial distribution of the TKE is intrinsically constraint by the wind gradient. A slight inclination (as somebody brushed it from left to right) in the bursts is also present. Some events show that turbulence is still maintained away from the surface (see Fig. 4a $t = 3.5 \text{ h}$ and $t = 5 \text{ h}$), leading to TKE that is decoupled from the surface. Here the flow is forced with a steady mean wind. Changing the forcing changes the gradient away from the surface and could provide room for the stochastic perturbations to appear at higher levels due to localised shear accelerations.

The impact of the randomised model on the temperature evolution is visualized in Fig. 5. It is evident that in the case of stochastic perturbations, the mixing is performed

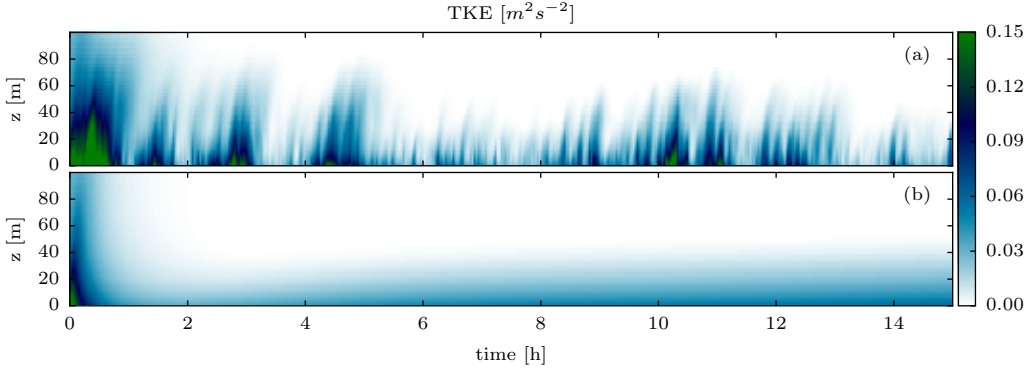


Figure 4. Temporal evolution of the profiles of TKE for a realization of the SURANS (a) and RANS (b) models. The color bar applies to both panels.

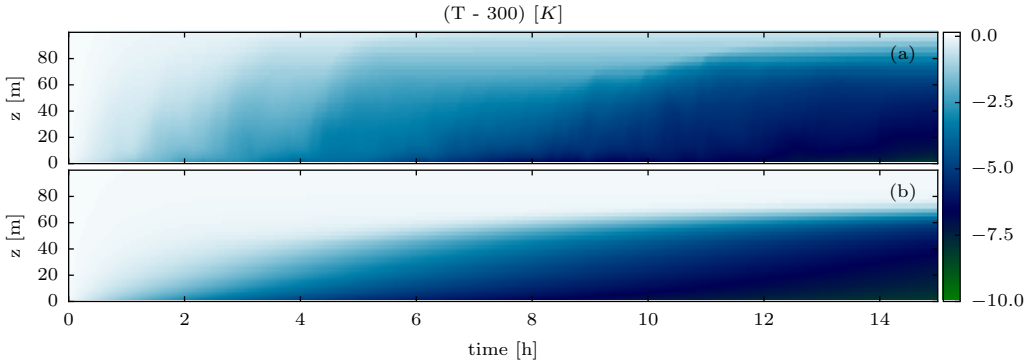


Figure 5. Temporal evolution of the temperature profiles for one realization of the SURANS (a) and RANS (b) models. The color bar is valid for both panels.

faster. The mixing rate is higher, and the temperature inversion is also shifted up and is less abrupt. The temperature profile changes its shape in an unsteady way (compare Fig. 5a to 5b), related to the activity of the intermittent burst periods (see Fig. 4a). The stochastic model shows a qualitatively different solution of the temperature inversion. The profiles of the dominant wind velocity component u are visualized in Fig. 6. A repeating pattern of the TKE bursts is visible in Fig. 6a, comparable to the pattern seen in Fig. 4a. The dominant stochastic turbulent diffusion dictates the boundary layer shape as a consequence of random mixing events. Figure 7 shows the evolution of the profiles for the Ri number. The SURANS model predicts a strongly unsteady local Ri number, but the bulk Ri number is computed for the layer between the z_0 level and $z = 80$ m. Deviations are found during random mixing events when the temperature profile is mixed sporadically, reducing the local bulk Ri number (compare with Fig. 5).

4.3 Variable Geostrophic Wind and Net Radiation

In the last case study, a time varying forcing scenario is considered, thereby studying the impact of the stochastic perturbations during transient states. The initial conditions are given in Sec. 3, and the simulation period is set to 30 hours, which is longer than the average nighttime. In this experiment, the focus lies on computing the transitions between weakly and strongly SBL, as in Maroneze et al. (2019); Acevedo et al.

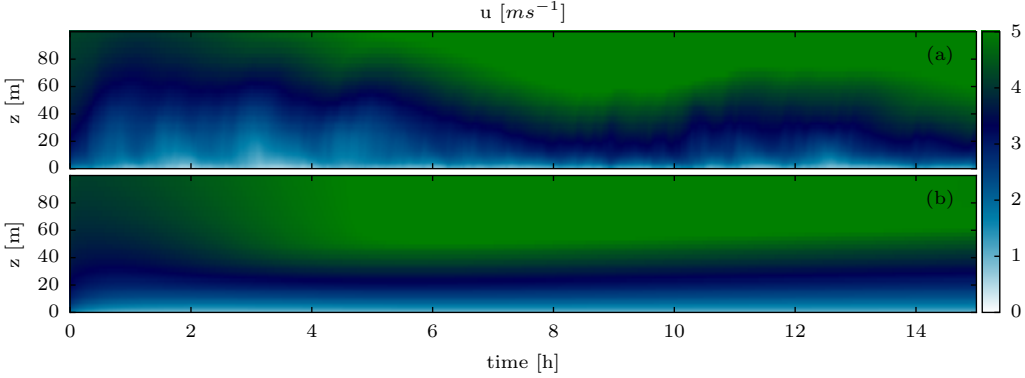


Figure 6. Temporal evolution of the wind profiles (u component) for one realization of the SURANS and RANS models. The color bar is valid for both panels.

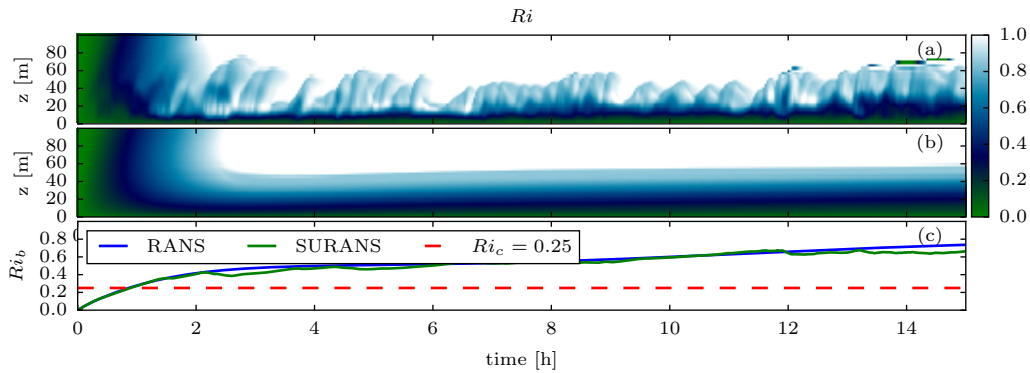


Figure 7. Temporal evolution of the Ri number profile for a realization of the SURANS (a) and RANS (b). The color bar applies to panels (a) and (b). Panel (c) shows the bulk Ri number calculated from the surface to $z = 80$ m.

(2021). The novelty of this study is that random mixing events are included in the model, representing unresolved features of the flow. The nonstationary forcing is chosen such that the geostrophic wind increases gradually at some given time, while the radiative cooling increases once from 0, to go back to a 0 value later in the simulation. The simulation thereby covers four possible forcing combinations, alternating in time as shown in Fig. 8a. The solver-specific settings for this experiment are given in Tab. 4 and the rest in Tab. 1.

The temporal evolution of the TKE at the height of $z = 9$ m is shown in Fig. 8b), with additional exerts showing the profiles for the variables e , θ and $U = \sqrt{u^2 + v^2}$ at three different times (note the arrows in Fig. 8b). The quantities visualised in Fig. 8 are:

- The 100 realizations of the SURANS model (gray, thin lines).
- The central tendency (solid red), estimated as the most probable value from the fitted distribution (see Fig. 3).
- The noise-free limit of the SURANS model. In this case, the stochastic equation is solved once with a sufficiently low value of the noise, such that the dynamical evolution can be considered deterministic (solid yellow line). The noise-free limit

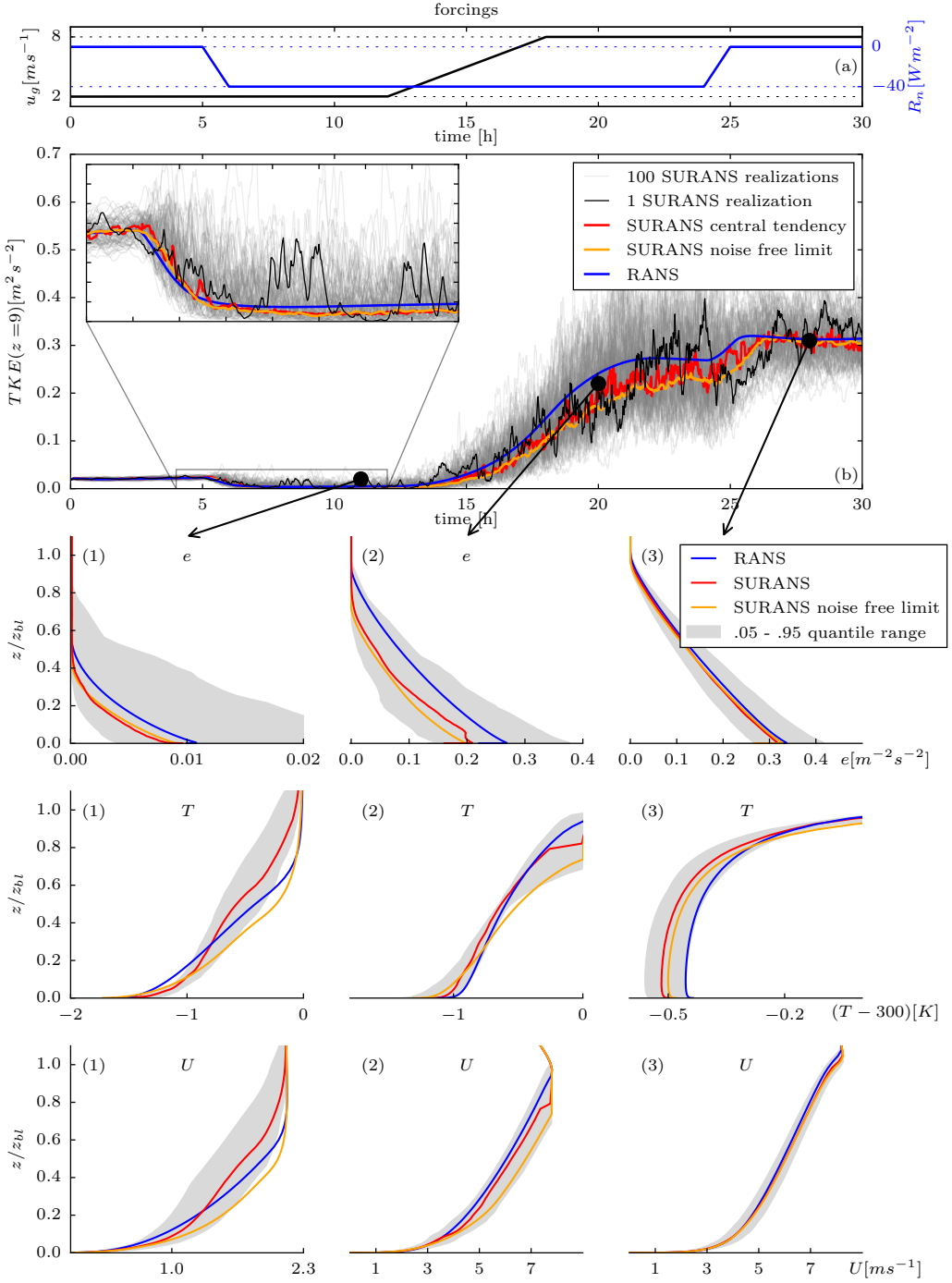


Figure 8. Solution of the SURANS model with variable forcing parameters R_n (net radiation) and the geostrophic wind u_g . The total simulation period is 30 hours. The nudging time scale is set to 5 hours. Panel (b) shows the evolution of TKE at 9 m for 100 realizations, marked with gray lines. The zoom area highlights the transition to stable stratification in weak winds by increasing net radiation. The evolution of the forcing is shown in a). The sub-images in b) show profiles of the variables at 3 different times marked with black dots in b). The SURANS profiles represent the central tendency, with the gray area showing the quantile range. The boundary layer height z_{bl} used for normalization is 50 m (first period), 200 m (second period), 240 m (third period).

Table 4. Relevant solver settings for the numerical study with unsteady forcing variables.

Description	Symbol	Value
Total simulation time [h]	T_end_h	30
Time step [s]	dt	2
Grid resolution (z grid)	Nz	100
Domain height [m]	H	300
Restoring temperature [K]	θ_s	300
Reference potential Temperature [K]	Θ_0	300
Net radiation [W m^{-2}]	R_n	variable (see Fig. 8a)
Geostrophic wind [m/s]	u_g	variable (see Fig. 8a)

377 is introduced to eliminate the effect of the difference between the MOST stabil-
 378 ity function and the deterministic steady-state of the prognostic Eq. (15) (the ex-
 379 pected value of the random variable). One realization of the SURANS model is
 380 emphasized to highlight the rare events during the stable low-wind conditions (solid
 381 black line).

- 382 • The prediction of the RANS model (solid blue line).

383 To study the impact of the applied perturbations, we first compare a solution of
 384 SURANS in the noise-free limit with the central tendency estimated from the 100 real-
 385 izations of the stochastic model (see yellow and red lines in Fig. 8). There are no sig-
 386 nificant differences in the TKE (see 8b and the corresponding profiles). However, there
 387 is a substantial impact of the applied perturbations on temperature and velocity pro-
 388 files. With stochasticity, the temperature is mixed more effectively during the stably strat-
 389 ified period and the mixing extends above the average boundary layer height (see Fig. 8
 390 panel (1)). The central tendency of the velocity profile experiences a deceleration com-
 391 pared to the noise-free limit. For higher geostrophic winds in the second visualised pe-
 392 riod, the perturbation of the turbulent diffusion is propagated to the top of the bound-
 393 ary layer (200 m), although the actual perturbations are limited at 50 m.

394 As a next step, we compare the results of the SURANS and the RANS models. The
 395 RANS solution (blue line) predicts higher levels of TKE than the central tendency (red
 396 line) obtained by the SURANS model, throughout the entire simulation. Despite this
 397 lower level of TKE simulated by the SURANS model, transport of temperature and ve-
 398 locity is enhanced (see Fig. 8 panels (1)). This nontrivial effect may result from non-equilibrium
 399 statistics in the stochastic formulation of the turbulent mixing length. The variability
 400 of results is visualised through the gray area in Figure 8, representing the 0.05 – 0.95
 401 quantile range of the 100 different model runs. For stable stratification (see Fig. 8 pan-
 402 el (1)), the quantile range for the TKE is asymmetrical, showing the largest spread clos-
 403 est to the surface. In neutral conditions, the quantile range is symmetrical (see Fig. 8
 404 panels (3)). The model ensemble spread for the TKE profile is significantly different than
 405 the ensemble spread for the temperature and velocity profiles. The largest ensemble spread
 406 for temperature and velocity profiles is found in the middle of the boundary layer, with
 407 lower spread at the surface and the boundary layer top.

408 Observing the individual simulation paths (see Fig. 8b thin gray lines), the impact
 409 of the random perturbations on the transition periods can be analysed. The inset in Fig.
 410 8b highlights a transition from neutral to stable stratification induced by the onset of
 411 radiative cooling. The central tendency and the noise-free limit of the SURANS model
 412 overlap during the transition. However, multiple individual realizations (thin gray lines)
 413 show a pronounced tendency to delay the transition rather than induce early transition.
 414 In contrast, by transitioning from low wind to high wind (see Fig. 8b from $t = 15$ to

415 $t = 20$), the solution paths can show both early and delayed transitions. The individual
 416 simulation paths also show that during this period where u_g increases, the variance
 417 in the TKE increases as well. When radiative cooling is interrupted (see $t = 25$ h), the
 418 variance reduces to some lower value. The reason for this is the parametrization of the
 419 noise term in the stochastic equation, which only scales with the Ri number. This scal-
 420 ing was identified by Boyko and Vercauteren (n.d.), but possibly other dependencies could
 421 be investigated.

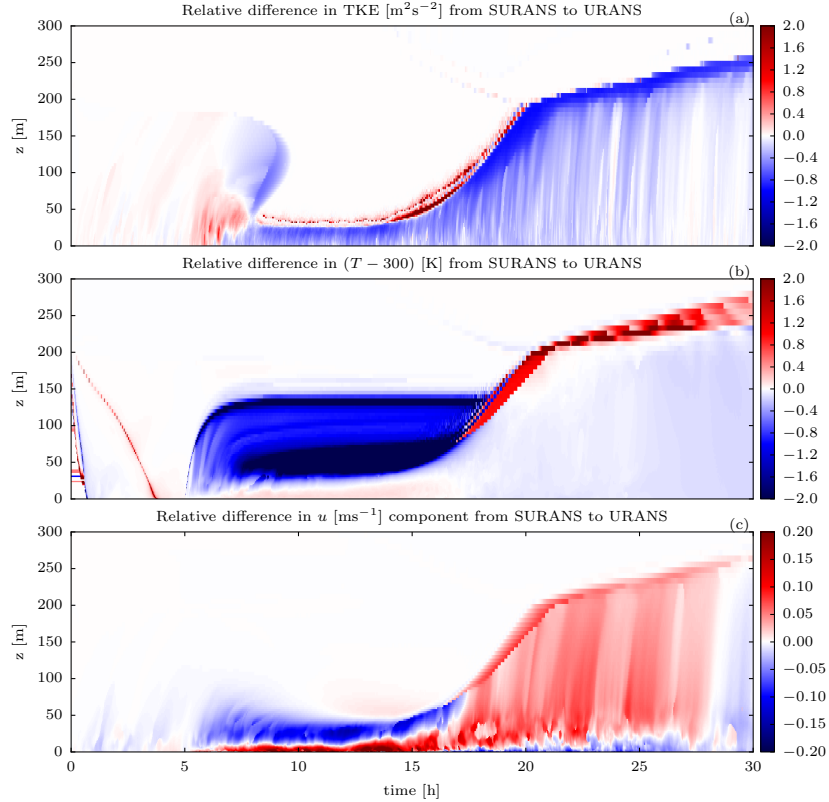


Figure 9. The relative difference in profiles between the SURANS (the central tendency of 100 realizations) and the RANS model according to the numerical study in Fig. 8. The red color denotes the area where the variables of the SURANS model have larger magnitude than those of the RANS model. The white color denotes no differences. Panel (a) shows the TKE, (b) the temperature ($-2 \text{ [K]} < (T - 300)[\text{K}] < 0 \text{ [K]}$), and (c) the dominant u component of the wind. The forcing variables change with time and are shown in Fig. 8a. Condition of stable stratification for $t \in (5, 15)$ h and condition of high wind pressure for $t \in (5, 15)$ h.

422 The relative differences in space and time of solutions obtained through the SURANS
 423 and RANS models are shown in Figure 9, where panel a shows the differences in TKE.
 424 The transition from blue to white color (no difference) indicates approximately the bound-
 425 ary layer height. The boundary layer grows after $t = 15$ h as the geostrophic wind is in-
 426 creased. For the time $t > 25$ h the radiative cooling is interrupted, and the central ten-
 427 dency of the SURANS model becomes very similar to the RANS solution. For the time
 428 $t > 6$ h the value of the TKE predicted by the SURANS model is 50% smaller than pre-
 429 dicted by RANS on average, indicating a shallower boundary layer (as seen in the TKE
 430 profiles of Fig. 8). Figure 9b shows the relative difference in the temperature. Within
 431 the boundary layer (where relative differences in TKE are found) the differences between

SURANS and RANS are insignificant. At the boundary layer top, the SURANS model deviates from the RANS solution. For the stably stratified conditions ($t \in (5, 15)$), the central tendency of the SURANS solution predicts almost a 200% lower value of the temperature than the RANS model for a large area above the boundary layer (see the blue area in Fig. 9b). At the same time, the differences at the surface are relatively small. This can be explained by the enhanced transport due to intermittent turbulence. By construction, the stochastic perturbations start to fade away above $z > 50$ m. At the same time, the boundary layer height is approximately 25 m, such that the stochastic perturbations determine the mixing of temperature. The red area at the top of the boundary layer in Fig. 9b for $t > 17$ h (the high-wind regime) means that the central tendency of the SURANS model is predicting an increased value of the temperature relative to the RANS model. Hence, the errors produced in the stable regime ($5 < t < 15$ h) are propagated into the high-wind regime ($t > 20$ h) at the boundary layer top. This findings suggest that the altered transport of temperature and possibly moisture (although not included in this model) may impact the creation of clouds in the early morning with increasing geostrophic winds.

5 Summary and conclusions

A stochastic stability equation, suggested by Boyko and Vercauteren (n.d.) to introduce a stochastic parameterisation of unsteady turbulence, was implemented and tested in this study. The previous data-driven analyses showed that the stochastic model for turbulent mixing could in principle accommodate both the short-term intermittent behaviour of turbulence and the long-term averaged mixing, as validated against field measurements. The stochastic model parameters in the SURANS model were found to scale with the local gradient Ri number (Boyko & Vercauteren, n.d.). As a result, the intermittent statistical properties of the modelled TKE are changing continuously as a function of flow stability. In this paper, the stochastic parameterisation was implemented in a SURANS single-column model extended from a RANS model with 1.5 closure. The stochastic stability equation can in principle also be used in a first-order closure model. The impact of the randomized model was evaluated through selected idealised numerical case studies with varying stability conditions. In the current implementation, the stochastic equation is confined to the lower portion of the boundary layer and is blended with a deterministic model above. It is unknown at this stage if the proposed closure is locally valid in the outer boundary layer.

The proposed framework was found to be numerically stable. In the strongly stable condition it is advisable to use an adaptive time stepping in the time integration to avoid abrupt numerical instabilities. These instabilities come from the strong stratification in combination with the stochastic events. Due to the randomness of the stochastic events it can happen that negative TKE is induced. Any mechanism preventing the solver to run negative TKE values is necessary for strongly stable conditions.

In neutral conditions, the stochastic parameterisation was found not to have a significant impact on the statistical properties of the modelled flow, simply introducing limited variability compared to the RANS reference model. Within the regime of strong stratification, the SURANS model adequately represents intermittent TKE patterns. The intermittent mixing events affect the boundary layer height. In conditions of weak stratification and large geostrophic wind speeds, the SURANS model appears to show unrealistically large variance, indicating that further model tuning may be necessary. For practical application it is advisable to limit the noise intensity in the stochastic stability equation by some critical geostrophic wind, for example. In stably stratified conditions, the SURANS model shows enhanced mixing properties in comparison to a RANS with a linear stability correction function. The temperature profile is mixed faster and reaches over larger heights. In comparison to the RANS solution, the stochastic model predicts lower temperature value just above the shallow, stably stratified boundary layer.

484 The effect of stochastic diffusion reaches beyond the limiting height of the perturbations.
 485 This results in qualitatively different profiles compared to the RANS solutions in the outer
 486 boundary layer. Furthermore, the boundary layer height becomes highly variable in strongly
 487 SBL and is determined by the random turbulent mixing events.

488 The presented SURANS model shows the potential to be used as an exploratory
 489 or even predictive tool. To investigate the use of the SSE for less idealized setups, fu-
 490 ture studies should validate the performance of the SURANS in controlled case studies
 491 using observational data.

492 6 Open Research

493 The computational software used in this study is publicly available at GitHub: <https://github.com/BoundaryLayerVercauteren/surans>
 494

495 Acknowledgments

496 We are grateful to Felix Oertel for his contribution to the development of the numeri-
 497 cal model, and to Ivan Bašták Ďurán with whom we had helpful discussions regarding
 498 the numerical stability of the code. The research was funded by the Deutsche Forschungs-
 499 gemeinschaft (DFG) through grant number VE 933/2-2.

500 References

- 501 Acevedo, O. C., Costa, F. D., Maroneze, R., Carvalho, A. D., Puhales, F. S.,
 502 & Oliveira, P. E. S. (2021, April). External controls on the transi-
 503 tion between stable boundary-layer turbulence regimes. *Quarterly Jour-*
 504 *nal of the Royal Meteorological Society*, qj.4027. Retrieved 2021-04-14,
 505 from <https://onlinelibrary.wiley.com/doi/10.1002/qj.4027> doi:
 506 10.1002/qj.4027
- 507 Acevedo, O. C., Mahrt, L., Puhales, F. S., Costa, F. D., Medeiros, L. E., & De-
 508 grazia, G. A. (2016). Contrasting structures between the decoupled and
 509 coupled states of the stable boundary layer. *Quarterly Journal of the Royal*
 510 *Meteorological Society*, 142(695), 693–702. Retrieved 2020-07-26, from
 511 <https://rmets.onlinelibrary.wiley.com/doi/abs/10.1002/qj.2693>
 512 doi: 10.1002/qj.2693
- 513 Alnæs, M., Blechta, J., Hake, J., Johansson, A., Kehlet, B., Logg, A., ... Wells,
 514 G. N. (2015). The FEniCS Project Version 1.5. *Archive of Numerical Software*,
 515 Vol 3. Retrieved from <http://journals.ub.uni-heidelberg.de/index.php/ans/article/view/20553> (Publisher: University Library Heidelberg) doi:
 516 10.11588/ANS.2015.100.20553
- 517 Anfossi, D., Oettl, D., Degrazia, G., & Goulart, A. (2005). An Analysis of Sonic
 518 Anemometer Observations In Low Wind Speed Conditions. *Boundary-Layer*
 519 *Meteorology*, 114(1), 179–203. Retrieved from <http://link.springer.com/article/10.1007/s10546-004-1984-4> (Publisher: Kluwer Academic Pub-
 520 lishers) doi: 10.1007/s10546-004-1984-4
- 521 Audouin, O., Roehrig, R., Couvreux, F., & Williamson, D. (2021). Modeling the
 522 GABLS4 Strongly-Stable Boundary Layer With a GCM Turbulence Param-
 523 eterization: Parametric Sensitivity or Intrinsic Limits? *Journal of Advances*
 524 *in Modeling Earth Systems*, 13(3), e2020MS002269. Retrieved 2021-10-21,
 525 from <https://onlinelibrary.wiley.com/doi/abs/10.1029/2020MS002269>
 526 (*eprint*: <https://onlinelibrary.wiley.com/doi/pdf/10.1029/2020MS002269>) doi:
 527 10.1029/2020MS002269
- 528 Baas, P., van de Wiel, B., Van der Linden, S., & Bosveld, F. (2018). From near-
 529 neutral to strongly stratified: Adequately modelling the clear-sky nocturnal

- boundary layer at Cabauw. *Boundary-Layer Meteorology*, 166(2), 217–238. (Publisher: Springer)
- Baas, P., van de Wiel, B. J., Van Meijgaard, E., Vignon, E., Genthon, C., van der Linden, S. J., & de Roode, S. R. (2019). Transitions in the wintertime near-surface temperature inversion at Dome C, Antarctica. *Quarterly Journal of the Royal Meteorological Society*, 145(720), 930–946. (Publisher: Wiley Online Library)
- Berner, J., Achatz, U., Batté, L., Bengtsson, L., CáMara, A. d. l., Christensen, H. M., ... Yano, J.-I. (2017, March). Stochastic Parameterization: Toward a New View of Weather and Climate Models. *Bulletin of the American Meteorological Society*, 98(3), 565–588. Retrieved 2022-12-12, from <https://journals.ametsoc.org/view/journals/bams/98/3/bams-d-15-00268.1.xml> (Publisher: American Meteorological Society Section: Bulletin of the American Meteorological Society) doi: 10.1175/BAMS-D-15-00268.1
- Blackadar, A. K. (1962, July). The vertical distribution of wind and turbulent exchange in a neutral atmosphere. *Journal of Geophysical Research*, 67(8), 3095–3102. Retrieved 2021-05-09, from <http://doi.wiley.com/10.1029/JZ067i008p03095> doi: 10.1029/JZ067i008p03095
- Boyko, V. (2022). *Data-driven modeling of intermittent turbulence in the stably stratified atmospheric boundary layer* (Unpublished doctoral dissertation). Freie Universität Berlin. (unpublished thesis)
- Boyko, V., & Vercauteren, N. (n.d.). A stochastic stability equation for unsteady turbulence in the stable boundary layer. *Quarterly Journal of the Royal Meteorological Society*, n/a(n/a). Retrieved from <https://rmets.onlinelibrary.wiley.com/doi/abs/10.1002/qj.4498> doi: <https://doi.org/10.1002/qj.4498>
- Boyko, V., & Vercauteren, N. (2020, November). Multiscale Shear Forcing of Turbulence in the Nocturnal Boundary Layer: A Statistical Analysis. *Boundary-Layer Meteorology*. Retrieved 2021-01-12, from <http://link.springer.com/10.1007/s10546-020-00583-0> doi: 10.1007/s10546-020-00583-0
- Cava, D., Mortarini, L., Anfossi, D., & Giostra, U. (2019, May). Interaction of Submeso Motions in the Antarctic Stable Boundary Layer. *Boundary-Layer Meteorology*, 171(2), 151–173. Retrieved 2021-08-10, from <http://link.springer.com/10.1007/s10546-019-00426-7> doi: 10.1007/s10546-019-00426-7
- Cuxart, J., Holtslag, A. A. M., Beare, R. J., Bazile, E., Beljaars, A., Cheng, A., ... Xu, K.-M. (2006, February). Single-Column Model Intercomparison for a Stably Stratified Atmospheric Boundary Layer. *Boundary-Layer Meteorology*, 118(2), 273–303. Retrieved 2020-10-14, from <http://link.springer.com/10.1007/s10546-005-3780-1> doi: 10.1007/s10546-005-3780-1
- Davy, R., & Esau, I. (2014, November). Global climate models' bias in surface temperature trends and variability. *Environmental Research Letters*, 9(11), 114024–9. Retrieved from <http://stacks.iop.org/1748-9326/9/i=11/a=114024?key=crossref.62a944a006fcfa4eb162e69a83af29733> (Publisher: IOP Publishing) doi: 10.1088/1748-9326/9/11/114024
- Delage, Y. (1974). A numerical study of the nocturnal atmospheric boundary layer. *Quarterly Journal of the Royal Meteorological Society*, 100(425), 351–364. Retrieved 2023-03-02, from <https://onlinelibrary.wiley.com/doi/abs/10.1002/qj.49710042507> (*eprint*: <https://onlinelibrary.wiley.com/doi/pdf/10.1002/qj.49710042507>) doi: 10.1002/qj.49710042507
- Derbyshire, S. (1999). Stable Boundary-Layer Modelling: Established Approaches and Beyond. *Boundary-Layer Meteorology*, 90(3), 423–446. Retrieved from <http://link.springer.com/10.1023/A:1001749007836> (Publisher: Kluwer Academic Publishers) doi: 10.1023/A:1001749007836
- Dunbar, T. M., Hanert, E., & Hogan, R. J. (2008, September). A One-Dimensional

- 587 Finite-Element Boundary-Layer Model with a Vertical Adaptive Grid.
 588 *Boundary-Layer Meteorology*, 128(3), 459–472. Retrieved 2021-05-24,
 589 from <http://link.springer.com/10.1007/s10546-008-9297-7> doi:
 590 10.1007/s10546-008-9297-7
- 591 Edwards, J. M., Beljaars, A. C. M., Holtslag, A. A. M., & Lock, A. P. (2020,
 592 December). Representation of Boundary-Layer Processes in Numerical
 593 Weather Prediction and Climate Models. *Boundary-Layer Meteorology*,
 594 177(2), 511–539. Retrieved 2021-08-24, from <https://doi.org/10.1007/s10546-020-00530-z> doi: 10.1007/s10546-020-00530-z
- 595 Esau, I., Tolstykh, M., Fadeev, R., Shashkin, V., Makhnorylova, S., Miles, V., &
 596 Melnikov, V. (2018, December). Systematic errors in northern Eurasian
 597 short-term weather forecasts induced by atmospheric boundary layer thick-
 598 ness. *Environmental Research Letters*, 13(12), 125009. Retrieved 2022-12-13,
 599 from <https://dx.doi.org/10.1088/1748-9326/aaecfb> (Publisher: IOP
 600 Publishing) doi: 10.1088/1748-9326/aaecfb
- 601 Garratt, J. R. (1994). The atmospheric boundary layer. *Earth-Science Reviews*,
 602 37(1-2), 89–134. (Publisher: Elsevier)
- 603 Grachev, A. A., Fairall, C. W., Persson, P. O. G., Andreas, E. L., & Guest,
 604 P. S. (2005, August). Stable Boundary-Layer Scaling Regimes: The
 605 Sheba Data. *Boundary-Layer Meteorology*, 116(2), 201–235. Retrieved
 606 2023-05-11, from <https://doi.org/10.1007/s10546-004-2729-0> doi:
 607 10.1007/s10546-004-2729-0
- 608 Holtslag, A. A. M., Svensson, G., Baas, P., Basu, S., Beare, B., Beljaars, A. C. M.,
 609 ... Van De Wiel, B. J. H. (2013, November). Stable Atmospheric Boundary
 610 Layers and Diurnal Cycles: Challenges for Weather and Climate Models. *Bul-
 611 letin of the American Meteorological Society*, 94(11), 1691–1706. Retrieved
 612 2020-07-26, from <https://journals.ametsoc.org/bams/article/94/11/1691/60301/Stable-Atmospheric-Boundary-Layers-and-Diurnal> doi:
 613 10.1175/BAMS-D-11-00187.1
- 614 Horsthemke, W. (1984). Noise Induced Transitions. *Non-Equilibrium Dynam-
 615 ics in Chemical Systems*, 150–160. Retrieved 2021-02-09, from https://link.springer.com/chapter/10.1007/978-3-642-70196-2_23 (Publisher:
 616 Springer, Berlin, Heidelberg) doi: 10.1007/978-3-642-70196-2_23
- 617 Kähnert, M., Sodemann, H., Remes, T. M., Fortelius, C., Bazile, E., & Esau, I.
 618 (2022, November). Spatial Variability of Nocturnal Stability Regimes in an
 619 Operational Weather Prediction Model. *Boundary-Layer Meteorology*. Re-
 620 tried 2022-11-21, from <https://doi.org/10.1007/s10546-022-00762-1>
 621 doi: 10.1007/s10546-022-00762-1
- 622 Køltzow, M., Casati, B., Bazile, E., Haiden, T., & Valkonen, T. (2019, August). An
 623 NWP Model Intercomparison of Surface Weather Parameters in the European
 624 Arctic during the Year of Polar Prediction Special Observing Period Northern
 625 Hemisphere 1. *Weather and Forecasting*, 34(4), 959–983. Retrieved 2023-
 626 02-07, from https://journals.ametsoc.org/view/journals/wefo/34/4/waf-d-19-0003_1.xml (Publisher: American Meteorological Society Section:
 627 Weather and Forecasting) doi: 10.1175/WAF-D-19-0003.1
- 628 Lan, C., Liu, H., Katul, G. G., Li, D., & Finn, D. (2022). Turbulence
 629 Structures in the Very Stable Boundary Layer Under the Influence of
 630 Wind Profile Distortion. *Journal of Geophysical Research: Atmo-
 631 spheres*, 127(20), e2022JD036565. Retrieved 2022-11-10, from <https://onlinelibrary.wiley.com/doi/abs/10.1029/2022JD036565> (.eprint:
 632 <https://onlinelibrary.wiley.com/doi/pdf/10.1029/2022JD036565>) doi:
 633 10.1029/2022JD036565
- 634 LeMone, M. A., Angevine, W. M., Bretherton, C. S., Chen, F., Dudhia, J., Fe-
 635 dorovich, E., ... Weil, J. C. (2018, January). 100 Years of Progress in Bound-
 636 ary Layer Meteorology. *Meteorological Monographs*, 59, 9.1–9.85. Retrieved
 637 640 641

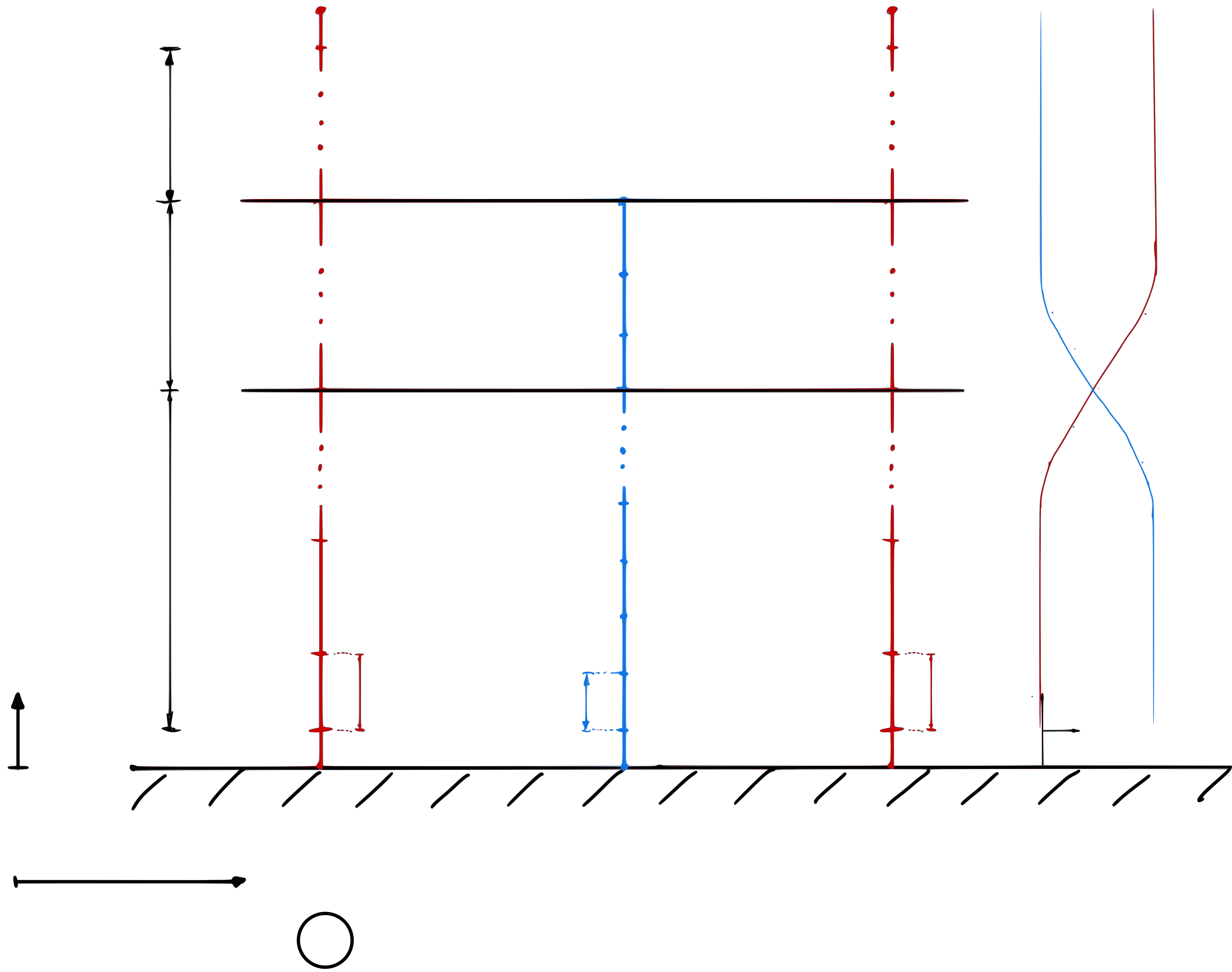
- from <http://journals.ametsoc.org/doi/10.1175/AMSMONOGRAPHSD-18-0013.1> doi: 10.1175/AMSMONOGRAPHSD-18-0013.1
- Logg, A., Mardal, K.-A., & Wells, G. (Eds.). (2012). *Automated Solution of Differential Equations by the Finite Element Method*. Springer Berlin Heidelberg. Retrieved from <https://doi.org/10.1007/978-3-642-23099-8> doi: 10.1007/978-3-642-23099-8
- Lord, G. J., Powell, C. E., & Shardlow, T. (2014). *An introduction to computational stochastic PDEs* (No. 50). New York, NY, USA: Cambridge University Press.
- Louis, J.-F. (1979, September). A parametric model of vertical eddy fluxes in the atmosphere. *Boundary-Layer Meteorology*, 17(2), 187–202. Retrieved from <https://link.springer.com/article/10.1007/BF00117978> (Publisher: Kluwer Academic Publishers) doi: 10.1007/BF00117978
- Mahrt, L. (2011, September). The Near-Calm Stable Boundary Layer. *Boundary-Layer Meteorology*, 140(3), 343–360. Retrieved 2020-07-26, from <http://link.springer.com/10.1007/s10546-011-9616-2> doi: 10.1007/s10546-011-9616-2
- Mahrt, L. (2014, January). Stably Stratified Atmospheric Boundary Layers. *Annual Review of Fluid Mechanics*, 46(1), 23–45. Retrieved 2020-07-26, from <http://www.annualreviews.org/doi/10.1146/annurev-fluid-010313-141354> doi: 10.1146/annurev-fluid-010313-141354
- Mahrt, L., & Bou-Zeid, E. (2020, June). Non-stationary Boundary Layers. *Boundary-Layer Meteorology*. Retrieved 2020-07-26, from <http://link.springer.com/10.1007/s10546-020-00533-w> doi: 10.1007/s10546-020-00533-w
- Maroneze, R., Acevedo, O. C., Costa, F. D., & Sun, J. (2019). Simulating the regime transition of the stable boundary layer using different simplified models. *Boundary-Layer Meteorology*, 170(2), 305–321. (Publisher: Springer)
- Mauritsen, T., Svensson, G., Zilitinkevich, S. S., Esau, I., Enger, L., & Grisogono, B. (2007, November). A Total Turbulent Energy Closure Model for Neutrally and Stably Stratified Atmospheric Boundary Layers. *Journal of Atmospheric Sciences*, 64(11), 4113–4126. Retrieved from <http://journals.ametsoc.org/doi/10.1175/2007JAS2294.1> doi: 10.1175/2007JAS2294.1
- Parente, A., Gorlé, C., van Beeck, J., & Benocci, C. (2011, September). A Comprehensive Modelling Approach for the Neutral Atmospheric Boundary Layer: Consistent Inflow Conditions, Wall Function and Turbulence Model. *Boundary-Layer Meteorology*, 140(3), 411–428. Retrieved 2021-02-10, from <http://link.springer.com/10.1007/s10546-011-9621-5> doi: 10.1007/s10546-011-9621-5
- Rodrigo, J. S., & Anderson, P. S. (2013, September). Investigation of the Stable Atmospheric Boundary Layer at Halley Antarctica. *Boundary-Layer Meteorology*, 148(3), 517–539. Retrieved 2020-10-14, from <http://link.springer.com/10.1007/s10546-013-9831-0> doi: 10.1007/s10546-013-9831-0
- Sandu, I., Beljaars, A., Bechtold, P., Mauritsen, T., & Balsamo, G. (2013, June). Why is it so difficult to represent stably stratified conditions in numerical weather prediction (NWP) models? *Journal of Advances in Modeling Earth Systems*, 5(2), 117–133. Retrieved 2020-07-26, from <http://doi.wiley.com/10.1002/jame.20013> doi: 10.1002/jame.20013
- Sanz Rodrigo, J., Churchfield, M., & Kosovic, B. (2017, February). A methodology for the design and testing of atmospheric boundary layer models for wind energy applications. *Wind Energy Science*, 2(1), 35–54. Retrieved 2021-05-09, from <https://wes.copernicus.org/articles/2/35/2017/> doi: 10.5194/wes-2-35-2017
- Scott, D. W. (2015). *Multivariate Density Estimation*. Wiley. Retrieved from <https://doi.org/10.1002/9781118575574> doi: 10.1002/9781118575574
- Sorjan, Z. (2012). A study of the stable boundary layer based on a single-column

- 697 K-theory model. *Boundary-layer meteorology*, 142(1), 33–53. (Publisher:
 698 Springer)
- 699 Steeneveld, G.-J., Nappo, C. J., & Holtslag, A. A. (2009, December). Estimation
 700 of orographically induced wave drag in the stable boundary layer during the
 701 CASES-99 experimental campaign. *Acta Geophysica*, 57(4), 857–881. Retrieved
 702 2023-05-11, from <https://doi.org/10.2478/s11600-009-0028-3>
 703 doi: 10.2478/s11600-009-0028-3
- 704 Stull, R. B. (1988). *An introduction to boundary layer meteorology* (Vol. 13).
 705 Springer Science & Business Media.
- 706 Sukoriansky, S., Galperin, B., & Staroselsky, I. (2005). A quasinormal scale elim-
 707 ination model of turbulent flows with stable stratification. *Physics of Fluids*,
 708 17(8), 085107. Retrieved from <http://link.aip.org/link/PHFLE6/v17/i8/p085107/s1&Agg=doi> doi: 10.1063/1.2009010
- 710 Sun, J., Burns, S. P., Lenschow, D. H., Banta, R., Newsom, R., Coulter, R., ... Hu,
 711 X.-Z. (2002, November). Intermittent Turbulence Associated with a Density
 712 Current Passage in the Stable Boundary Layer. *Boundary-Layer Meteorology*,
 713 105(2), 199–219. Retrieved 2021-08-10, from <http://link.springer.com/10.1023/A:1019969131774> doi: 10.1023/A:1019969131774
- 714 Tjernström, M., Žagar, M., Svensson, G., Cassano, J. J., Pfeifer, S., Rinke, A.,
 715 ... Shaw, M. (2005, November). Modelling the Arctic Boundary Layer: An Evaluation
 716 of Six Arcmip Regional-Scale Models using Data from the Sheba Project. *Boundary-Layer Meteorology*, 117(2), 337–381. Retrieved
 717 2023-02-07, from <https://doi.org/10.1007/s10546-004-7954-z> doi:
 718 10.1007/s10546-004-7954-z
- 719 van de Wiel, B. J. H., & Moene, A. F. (2003). Intermittent turbulence in
 720 the stable boundary layer over land. Part III: A classification for observa-
 721 tions during CASES-99. *Journal of Atmospheric Sciences*, 60(20), 2509–
 722 2522. Retrieved from [http://journals.ametsoc.org/doi/pdf/10.1175/1520-0469\(2003\)060%3C2509%3AITITSB%3E2.0.CO%3B2](http://journals.ametsoc.org/doi/pdf/10.1175/1520-0469(2003)060%3C2509%3AITITSB%3E2.0.CO%3B2)
- 723 Van de Wiel, B. J. H., Moene, A. F., Jonker, H. J. J., Baas, P., Basu, S., Donda,
 724 J. M. M., ... Holtslag, A. A. M. (2012, November). The Minimum Wind
 725 Speed for Sustainable Turbulence in the Nocturnal Boundary Layer. *Journal of the Atmospheric Sciences*, 69(11), 3116–3127. Retrieved 2021-11-15, from <https://journals.ametsoc.org/doi/10.1175/JAS-D-12-0107.1> doi:
 10.1175/JAS-D-12-0107.1
- 726 Van de Wiel, B. J. H., Vignon, E., Baas, P., van Hooijdonk, I. G. S., van der
 727 Linden, S. J. A., Antoon van Hooft, J., ... Genthon, C. (2017, April). Regime
 728 Transitions in Near-Surface Temperature Inversions: A Conceptual
 729 Model. *Journal of the Atmospheric Sciences*, 74(4), 1057–1073. Retrieved
 730 2020-07-26, from <https://journals.ametsoc.org/jas/article/74/4/1057/342605/Regime-Transitions-in-NearSurface-Temperature> doi:
 731 10.1175/JAS-D-16-0180.1
- 732 Vercauteren, N., Mahrt, L., & Klein, R. (2016, July). Investigation of interactions
 733 between scales of motion in the stable boundary layer: Interactions between
 734 Scales of Motion in the Stable Boundary Layer. *Quarterly Journal of the Royal
 735 Meteorological Society*, 142(699), 2424–2433. Retrieved 2020-07-26, from
 736 <http://doi.wiley.com/10.1002/qj.2835> doi: 10.1002/qj.2835
- 737 Želi, V., Brethouwer, G., Wallin, S., & Johansson, A. V. (2019). Consistent
 738 boundary-condition treatment for computation of the atmospheric bound-
 739 ary layer using the explicit algebraic reynolds-stress model. *Boundary-Layer
 740 Meteorology*, 171(1), 53–77. (Publisher: Springer)
- 741 Zilitinkevich, S. S., Elperin, T., Kleoorin, N., & Rogachevskii, I. (2007, September).
 742 Energy- and flux-budget (EFB) turbulence closure model for stably stratified
 743 flows. Part I: steady-state, homogeneous regimes. *Boundary-Layer Meteorol-
 744 ogy*, 125(2), 167–191. Retrieved 2021-09-05, from <http://link.springer.com/10.1007/s10546-007-9250-2>

752

[.com/10.1007/s10546-007-9189-2](https://doi.org/10.1007/s10546-007-9189-2) doi: 10.1007/s10546-007-9189-2

Figure 1.



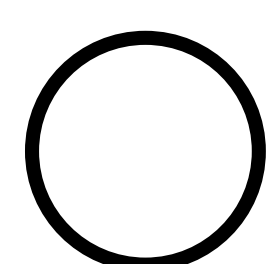
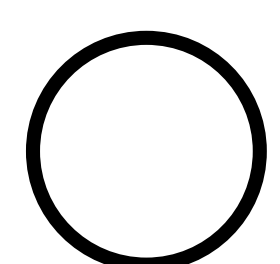
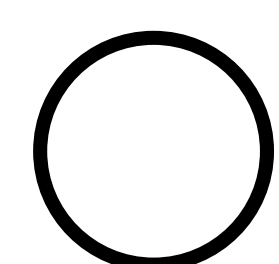
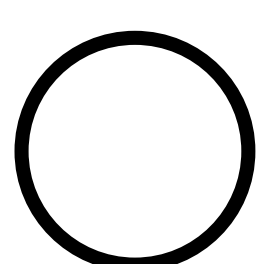


Figure 2.

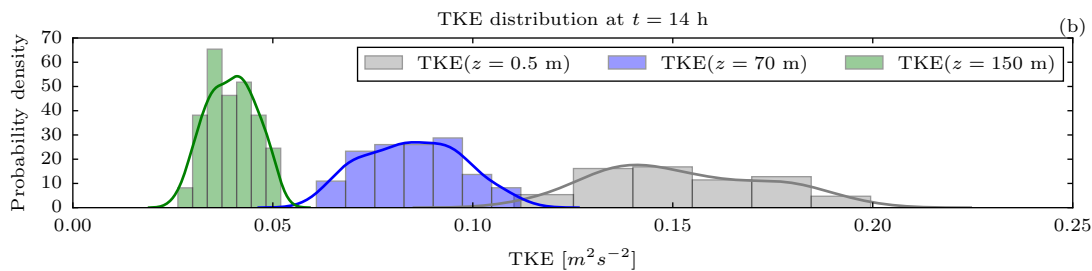
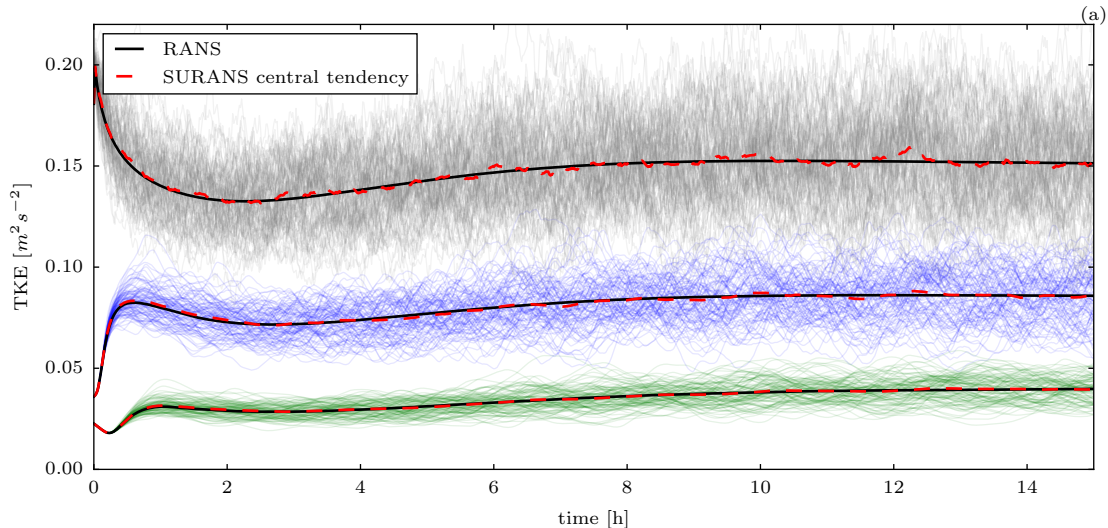


Figure 3.

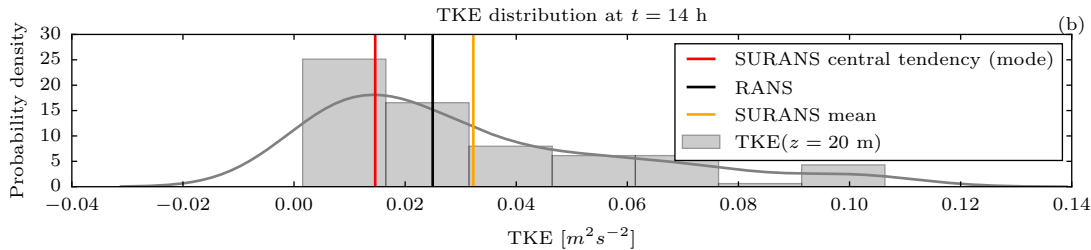
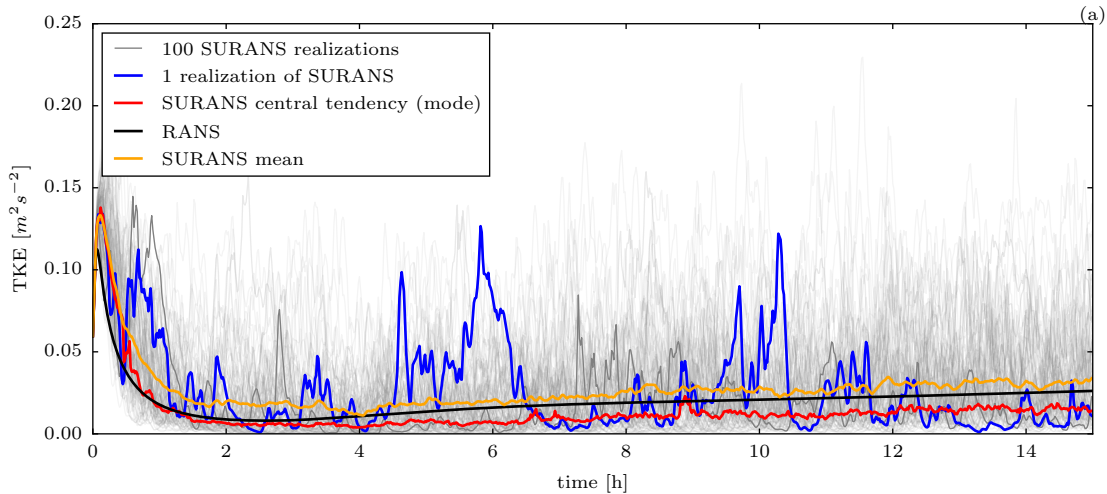


Figure 4.

TKE [$m^2 s^{-2}$]

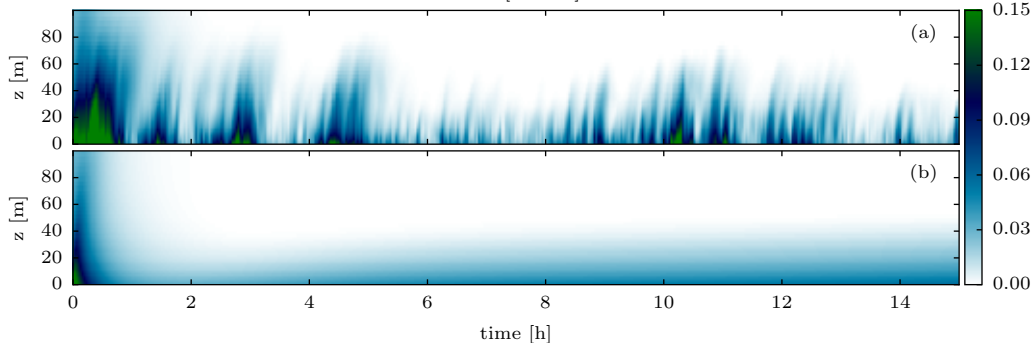


Figure 5.

$(T - 300) [K]$

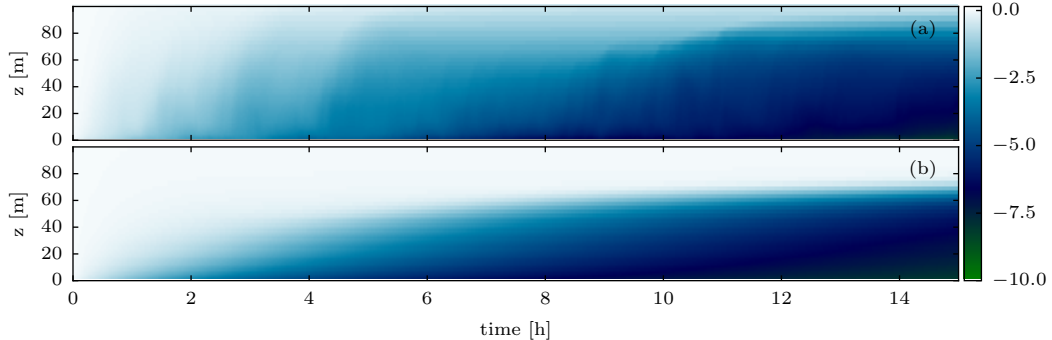


Figure 6.

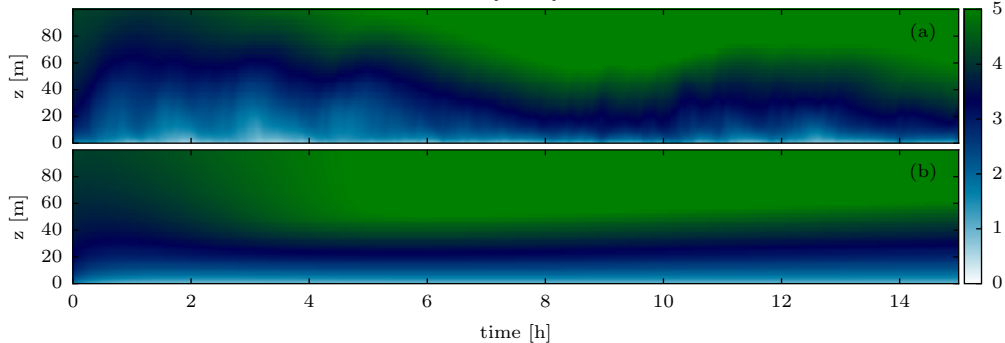
$u \ [ms^{-1}]$ 

Figure 7.

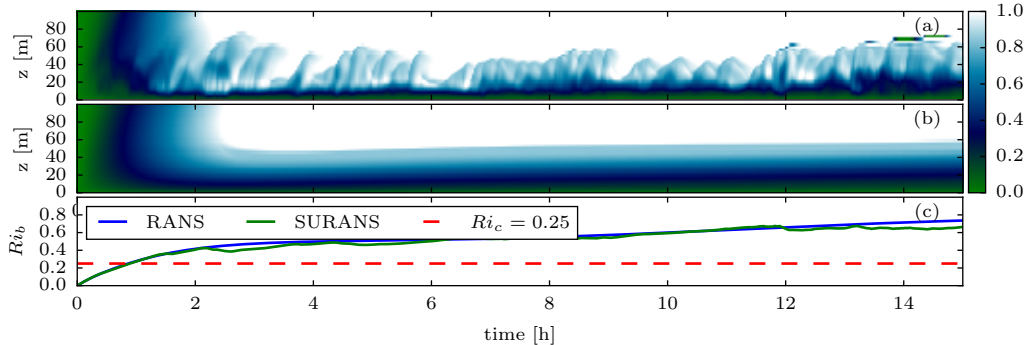
Ri 

Figure 8.

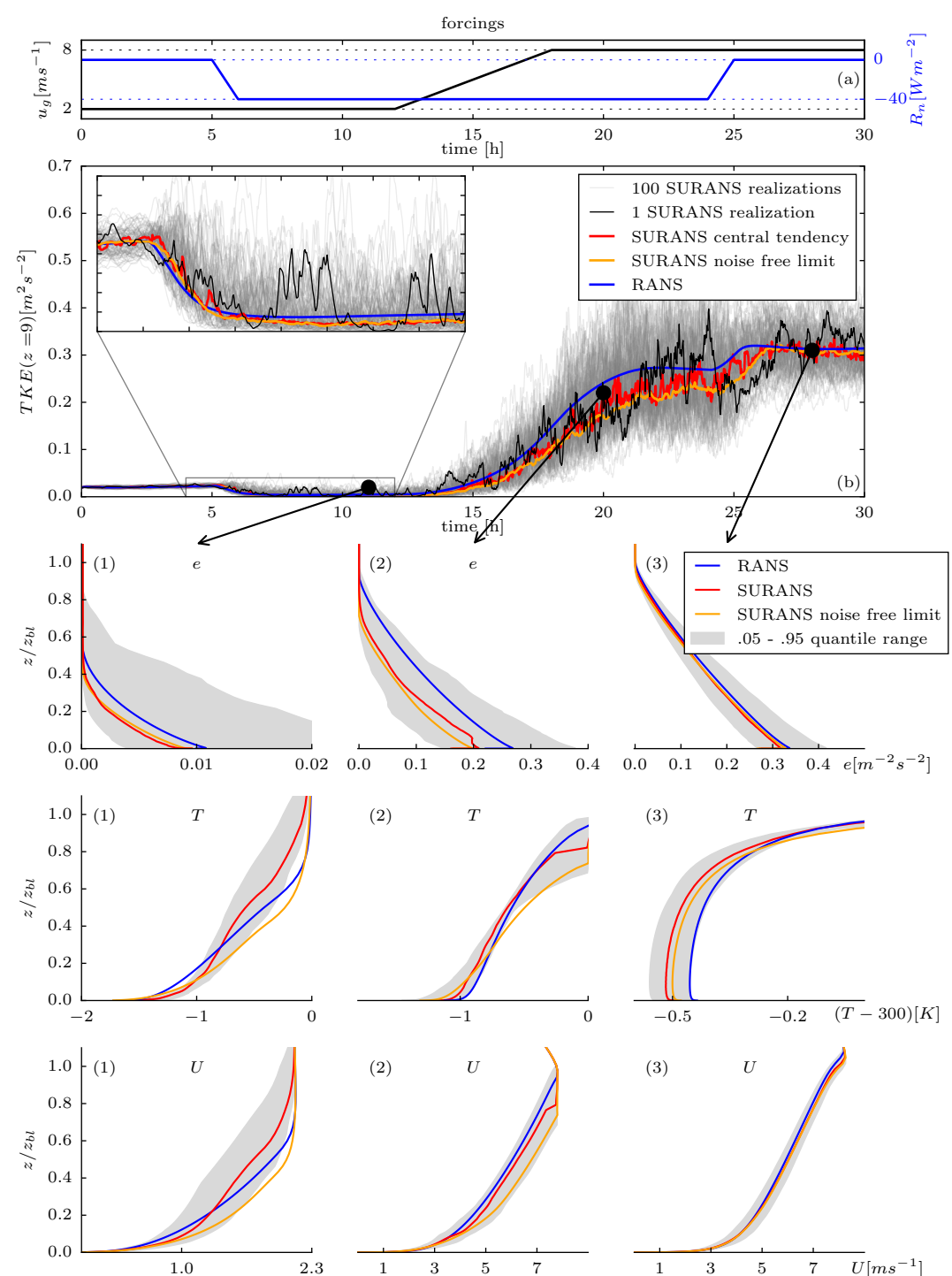
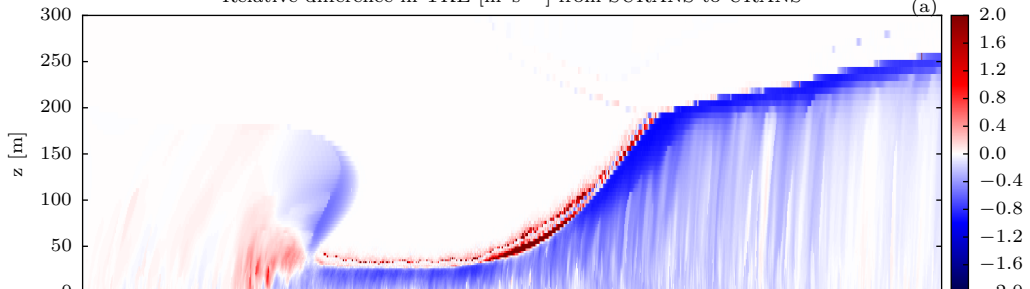


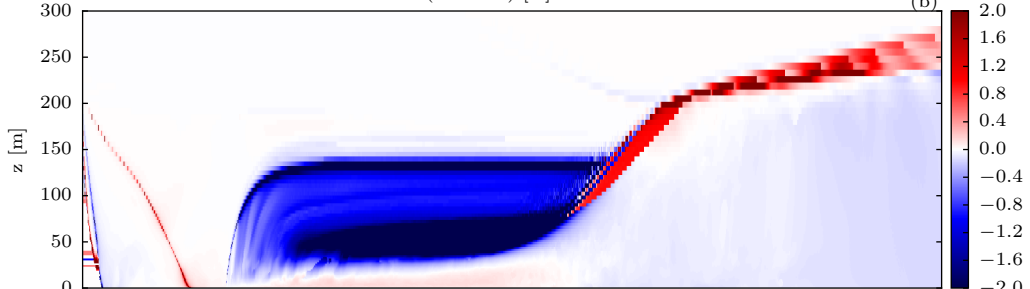
Figure 9.

Relative difference in TKE [m^2s^{-2}] from SURANS to URANS

(a)

Relative difference in $(T - 300)$ [K] from SURANS to URANS

(b)

Relative difference in u [ms^{-1}] component from SURANS to URANS

(c)

